Collisionless damping of zonal flows in helical systems

H. Sugama and T.-H. Watanabe
National Institute for Fusion Science, Graduate University for Advanced Studies, Toki 509-5292, Japan

(Received 12 September 2005; accepted 11 November 2005; published online 10 January 2006)

Collisionless time evolution of zonal flows in helical systems is investigated. An analytical expression describing the collisionless response of the zonal-flow potential to the initial potential and a given turbulence source is derived from the gyrokinetic equations combined with the quasineutrality condition. The dispersion relation for the geodesic acoustic mode (GAM) in helical systems is derived from the short-time response kernel for the zonal-flow potential. It is found that helical ripples in the magnetic-field strength as well as finite orbit widths of passing ions enhance the GAM damping. The radial drift motions of particles trapped in helical ripples cause the residual zonal-flow level in the collisionless long-time limit to be lower for longer radial wavelengths and deeper helical ripples. On the other hand, a high-level zonal-flow response, which is not affected by helical-ripple-trapped particles, can be maintained for a longer time by reducing their radial drift velocity. This implies a possibility that helical configurations optimized for reducing neoclassical ripple transport can simultaneously enhance zonal flows which lower anomalous transport. The validity of our analytical results is verified by gyrokinetic Vlasov simulation. © *2006 American Institute of Physics*. [DOI: 10.1063/1.2149311]

I. INTRODUCTION

Zonal flows are intensively investigated in the fusion research as an attractive mechanism for realizing a good plasma confinement.[1] A collisionless long-time behavior of zonal flows in tokamaks was theoretically investigated by Rosenbluth and Hinton[2] and their theory was extended to helical systems in our previous work.[3] In these theories, the ion temperature gradient (ITG) turbulence[4] is treated as a known source and the response kernel, which relates the zonal-flow potential to the source as well as represents dependence on an initially given zonal flow, is analytically derived. They showed that the initial zonal flow is not fully damped by collisionless processes but it approaches a finite value. It was verified by collisionless gyrokinetic simulations[5,6] that the zonal flow, which is added initially as an impulse, shows the convergence to the theoretically predicted value after oscillations of the geodesic acoustic mode[7] (GAM) are damped.

In the present paper, we extend our previous theory to give a complete description of collisionless time dependence of the zonal-flow potential by combining the long-time evolution with short-time behaviors such as the GAM oscillations. The GAM was first predicted by Winsor *et al.*[7] based on the fluid model. The GAM oscillations are observed experimentally by measuring the radial electric field in both tokamaks and helical systems.[8,9] Drift kinetic evaluations of frequencies and damping rates of the GAM in tokamaks were done by Lebedev *et al.*[10] and by Novakovskii *et al.*[11] Recently, Watari *et al.*[12] derived the dispersion relation for the GAM in helical systems based on the drift kinetic equation although they neglected a part of the electrostatic potential which depends on the poloidal and toroidal angles so that their dispersion relation shows a slight difference from that of Lebedev *et al.*[10] in the collisionless tokamak limit. Also, all the above-mentioned drift kinetic studies assume the radial widths of ion drift orbits to be negligibly smaller than the radial wavelength of the potential and their local drift kinetic models do not include the magnetic drift term of the perturbed distribution function that the gyrokinetic equation does. Just recently, based on the gyrokinetic theory and simulation, Sugama and Watanabe showed that the collisionless damping of the GAM in tokamaks is considerably strengthened by the finite-orbit-width (FOW) effect of passing ions.[13] This rapid damping of the GAM was also observed in the global drift kinetic simulation done by Satake *et al.*[14] Here, we also take account of the FOW effect as well as the helical geometry to derive the GAM dispersion relation from the analytically derived short-time response kernel for the zonal-flow potential in helical systems. In the tokamak case with no FOW effect, our GAM dispersion relation coincides with the collisionless result of Lebedev *et al.*[10]

In helical configurations, the radial drift motions of particles trapped in helical ripples yield neoclassical ripple transport in the weak collisionality regime.[15,16] Here, we argue that this radial drift of the helical-ripple-trapped particles also causes a significant influence on the long-time zonal-flow behavior and accordingly on the anomalous transport in helical systems. Our study suggests that helical configurations optimized for reduction of the neoclassical ripple transport may simultaneously lower the anomalous transport through enhancing the zonal-flow level. In fact, it is observed in the large helical device[17] (LHD) that not only neoclassical but also anomalous transport is reduced by the inward shift of the magnetic axis which decreases the radial drift of helical-ripple-trapped particles but increases the unfavorable magnetic curvature to destabilize pressure-gradient-driven instabilities such as the ITG mode.[18–20]

In this work, we also verify the validity of our theoretical predictions by a recently developed gyrokinetic Vlasov (GKV) simulation code[6] that can resolve detailed structures of the gyrocenter distribution function on the phase space. Here, we do not treat collisional decay of zonal flows, which occurs in the long course of time[21] although the residual zonal flows in a collisionless time scale are still regarded as critical factors to regulate the turbulent transport.

The rest of this paper is organized as follows. In Sec. II basic equations for describing zonal flows in helical systems are given. We use the gyrokinetic equations and the quasineutrality condition to determine the zonal-flow electrostatic potential. In Secs. III and IV, we describe the short- and long-time collisionless behaviors of the zonal-flow potential, respectively. It is shown in Sec. III how the GAM frequency and damping rate depend on the magnetic geometry and the FOW effect of passing ions. We see in Sec. IV that the residual zonal-flow level in the long-time limit is strongly influenced by the radial drift of helical-ripple-trapped particles. Then, in Sec. V, we combine the results from Secs. III and IV to obtain a complete expression for the collisionless time evolution of the zonal-flow potential. In Sec. VI gyrokinetic-Vlasov-simulation results on the zonal-flow evolution and on the velocity-space gyrocenter distribution are compared with our theoretical predictions. Finally, conclusions are given in Sec. VII. Appendix A shows in detail how the short-time zonal-flow behaviors such as the GAM oscillations are formulated by using the Fourier and Laplace transforms of the basic equations.

II. BASIC EQUATIONS

We use the toroidal coordinates (r,θ,ζ), where r, θ, and ζ denote the flux-surface label, the poloidal angle, and the toroidal angle, respectively. The magnetic field is written as $\mathbf{B}=\nabla\psi(r)\times\nabla(\theta-\zeta/q(r))$, where $2\pi\psi(r)$ is equal to the toroidal flux within the flux surface labeled r and $q(r)$ represents the safety factor. Following Shaing and Hokin,[16] we here consider helical systems with the magnetic-field strength written by a function of poloidal and toroidal angles (its r dependence is not shown here for simplicity) as

$$B = B_0\Bigg[1-\epsilon_{10}\cos\theta-\epsilon_{L0}\cos(L\theta) - \sum_{|n|\leqslant n_{\max}}\epsilon_h^{(n)}\cos\{(L+n)\theta-M\zeta\}\Bigg] = B_0[1-\epsilon_T(\theta)-\epsilon_H(\theta)\cos\{L\theta-M\zeta+\chi_H(\theta)\}], \tag{1}$$

where

$$\epsilon_T(\theta)=\epsilon_{10}\cos\theta+\epsilon_{L0}\cos(L\theta),$$

$$\epsilon_H(\theta)=\sqrt{C^2(\theta)+D^2(\theta)},$$

$$\chi_H(\theta)=\arctan[D(\theta)/C(\theta)], \tag{2}$$

$$C(\theta)=\sum_{|n|\leqslant n_{\max}}\epsilon_h^{(n)}\cos(n\theta),$$

$$D(\theta)=\sum_{|n|\leqslant n_{\max}}\epsilon_h^{(n)}\sin(n\theta),$$

and $M(L)$ is the toroidal (main poloidal) period number of the helical field. For the LHD, $L=2$ and $M=10$ while, for the compact helical system (CHS),[8] $L=2$ and $M=8$. Here, we assume that $L/(qM)\ll 1$. Multiple-helicity effects can be included in the function $\epsilon_H(\theta)$.

The gyrokinetic equation[22] for the zonal-flow component with the perpendicular wave-number vector $\mathbf{k}_\perp=k_r\nabla r$ is given by

$$\left(\frac{\partial}{\partial t}+v_\parallel\mathbf{b}\cdot\nabla+i\omega_D\right)g_{\mathbf{k}_\perp}=\frac{e}{T}F_0J_0(k_\perp\rho)\frac{\partial\phi_{\mathbf{k}_\perp}}{\partial t}+S_{\mathbf{k}_\perp}F_0, \tag{3}$$

where F_0 is the local equilibrium distribution function that takes the Maxwellian form, $J_0(k_\perp\rho)$ is the zeroth-order Bessel function, $\rho=v_\perp/\Omega$ is the gyroradius, and $\Omega=eB/(mc)$ is the gyrofrequency. Here, subscripts to represent particle species are dropped for simplicity. In Eq. (3), $g_{\mathbf{k}_\perp}$ is regarded as a function of independent variables (r,θ,ζ,w,μ), where $w\equiv\frac{1}{2}mv^2$ and $\mu\equiv mv_\perp^2/(2B)$ represent the kinetic energy and the magnetic moment, respectively. The gyrokinetic equation given in Eq. (3) is based on the ballooning representation[23] to describe the local structure of perturbations with much smaller perpendicular wave lengths than equilibrium scale lengths. We should also note that, for the perpendicular wave-number vector $\mathbf{k}_\perp=k_r\nabla r$ in the radial direction, the gyrokinetic equation does not explicitly contain such macroscale lengths as density and temperature gradient scale lengths. Then, the thermal gyroradius $(T/m)^{1/2}/\Omega$ is useful to normalize the radial wave number k_r of local perturbations as seen later. The equilibrium distribution function F_0 is assumed to be given by the local Maxwellian and the perturbed *particle* distribution function $\delta f_{\mathbf{k}_\perp}$ is written in terms of the electrostatic potential $\phi_{\mathbf{k}_\perp}$ and the solution $g_{\mathbf{k}_\perp}$ of Eq. (3) as

$$\delta f_{\mathbf{k}_\perp}=-\frac{e\phi_{\mathbf{k}_\perp}}{T}F_0+g_{\mathbf{k}_\perp}e^{-i\mathbf{k}_\perp\cdot\boldsymbol{\rho}}, \tag{4}$$

where $\boldsymbol{\rho}=\mathbf{b}\times\mathbf{v}/\Omega$. The drift frequency ω_D is defined by $\omega_D\equiv\mathbf{k}_\perp\cdot\mathbf{v}_d\equiv k_rv_{dr}$, where $v_{dr}=\mathbf{v}_d\cdot\nabla r$ is the radial component of the gyrocenter-drift velocity. In the present work, we define the radial coordinate r by $\psi=B_0r^2/2$. The source term

$S_{\mathbf{k}_\perp}F_0$ on the right-hand side of Eq. (3) represents the $\mathbf{E}\times\mathbf{B}$ nonlinearity and is written as $S_{\mathbf{k}_\perp}F_0 = (c/B)\Sigma_{\mathbf{k}'_\perp+\mathbf{k}''_\perp=\mathbf{k}_\perp}[\mathbf{b}\cdot(\mathbf{k}'_\perp\times\mathbf{k}''_\perp)]J_0(k'_\perp\rho)\phi_{\mathbf{k}'_\perp}g_{\mathbf{k}''_\perp}$.

The perturbed *gyrocenter* distribution function $\delta f^{(g)}_{\mathbf{k}_\perp}$ is given by

$$\delta f^{(g)}_{\mathbf{k}_\perp} = -J_0(k_\perp\rho)\frac{e\phi_{\mathbf{k}_\perp}}{T}F_0 + g_{\mathbf{k}_\perp}. \tag{5}$$

The perturbed gyrocenter distribution function $\delta f^{(g)}_{\mathbf{k}_\perp}$ and the nonadiabatic part $g_{\mathbf{k}_\perp}$ are independent of the gyrophase although the perturbed particle distribution function $\delta f_{\mathbf{k}_\perp}$ depends on it as seen from the factor $e^{-i\mathbf{k}_\perp\cdot\boldsymbol{\rho}}$ on the right-hand side of Eq. (4). Using Eqs. (4) and (5), we obtain

$$\delta f_{\mathbf{k}_\perp} = \delta f^{(g)}_{\mathbf{k}_\perp}e^{-i\mathbf{k}_\perp\cdot\rho} - \frac{e\phi_{\mathbf{k}_\perp}}{T}F_0[1-J_0(k_\perp\rho)e^{-i\mathbf{k}_\perp\cdot\boldsymbol{\rho}}]. \tag{6}$$

On the right-hand side of Eq. (6), the factor $e^{-i\mathbf{k}_\perp\cdot\rho}$ in the first term results from the difference between the particle and gyrocenter positions while the second group of terms represents the polarization, that is the variation of the particle distribution due to the potential perturbation. The gyrokinetic equation is rewritten in terms of $\delta f^{(g)}_{\mathbf{k}_\perp}$ as

$$\left(\frac{\partial}{\partial t} + v_\parallel\mathbf{b}\cdot\nabla + i\omega_D\right)\delta f^{(g)}_{\mathbf{k}_\perp} = -(v_\parallel\mathbf{b}\cdot\nabla + i\omega_D)\left(F_0J_0(k_\perp\rho)\frac{e\phi_{\mathbf{k}_\perp}}{T}\right) + S_{\mathbf{k}_\perp}F_0. \tag{7}$$

FOW effects are included in $i\omega_D\delta f^{(g)}_{\mathbf{k}_\perp}$ on the left-hand side of Eq. (7), which represents the rate of change of the perturbed gyrocenter distribution function $\delta f^{(g)}_{\mathbf{k}_\perp}$ due to the radial gyrocenter drift. This term is neglected in the conventional linearized drift kinetic equation, where the small-orbit-width limit is considered.

The electrostatic potential $\phi_{\mathbf{k}_\perp}$ is determined by the quasineutrality condition,

$$-n_0\frac{e\phi_{\mathbf{k}_\perp}}{T_i} + \int d^3v J_0 g_{i\mathbf{k}_\perp} = n_0\frac{e\phi_{\mathbf{k}_\perp}}{T_e} + \int d^3v g_{e\mathbf{k}_\perp}, \tag{8}$$

where the subscripts representing to ions (i) and electrons (e) are explicitly shown and the small-electron-gyroradius limit $k_\perp\rho_e\to 0$ is considered. Equation (8) is also rewritten as

$$\int d^3v J_0 f^{(g)}_{i\mathbf{k}_\perp} - n_0\frac{e\phi_{\mathbf{k}_\perp}}{T_i}[1-\Gamma_0(b)] = \int d^3v\delta f_{e\mathbf{k}_\perp}, \tag{9}$$

where $b\equiv k_\perp^2T_i/(m_i\Omega_i)$ and $\Gamma_0(b)\equiv I_0(b)e^{-b}$ are used and I_0 denotes the zeroth-order modified Bessel function. In the following two sections, short- and long-time behaviors of the zonal-flow potential are investigated by analytically solving the basic equations presented in this section.

When the initial gyrocenter distribution functions $\delta f^{(g)}_{a\mathbf{k}_\perp}(t=0)$ and the past history of the source terms $S_{a\mathbf{k}_\perp}(t')(a=i,e)$ are given, the gyrocenter distribution functions $\delta f^{(g)}_{a\mathbf{k}_\perp}(t)$ at an arbitrary time $t>0$ are determined by solving Eqs. (7) and (9) [note that the initial potential $\phi_{\mathbf{k}_\perp}(t=0)$ is immediately given in terms of $\delta f^{(g)}_{a\mathbf{k}_\perp}(t=0)$ by using Eq. (9)]. Examining the properties of these equations, we find that, in the static magnetic field, the response of $\delta f^{(g)}_{a\mathbf{k}_\perp}(t)$ to $\delta f^{(g)}_{a'\mathbf{k}_\perp}(t=0)$ and $S_{a'\mathbf{k}_\perp}(t')$ $(a,a'=i,e;0\leqslant t'\leqslant t)$ should take the form

$$\delta f^{(g)}_{a\mathbf{k}_\perp}(t) = \sum_{a'=i,e}\left[U_{aa'}(t)\delta f^{(g)}_{a'\mathbf{k}_\perp}(0) + \int_0^t dt' U_{aa'}(t-t')F_{a'0}S_{a'\mathbf{k}_\perp}(t')\right]. \tag{10}$$

Here, it should be noted that, once the linear operators (or propagators) $U_{aa'}(t)(a,a'=i,e)$, which relate $\delta f^{(g)}_{a\mathbf{k}_\perp}(t)$ to $\delta f^{(g)}_{a'\mathbf{k}_\perp}(0)$, are known, we can immediately obtain the kernels in the time integration representing the response to $F_{a'0}S_{a'\mathbf{k}_\perp}(t')$ by replacing the time argument t with $t-t'$. In other words, the solution of the linear initial-value problem is equivalent to the linear responses to the source terms. Substituting Eq. (10) into Eq. (9), we have

$$\frac{e\phi_{\mathbf{k}_\perp}(t)}{T_i} = \frac{1}{n_0[1-\Gamma_0(b)]}\sum_{a=i,e}\left[N_a(t)\delta f^{(g)}_{a\mathbf{k}_\perp}(0) + \int_0^t dt' N_a(t-t')F_{a0}S_{a\mathbf{k}_\perp}(t')\right], \tag{11}$$

where $N_a(t)\equiv\int d^3vU_{ia}(t) - \int d^3vU_{ea}(t)$.

III. GAM OSCILLATIONS

In the present section, we are concerned with rapidly varying fluctuations in the GAM frequency range. The GAM is a normal mode of the surface-potential oscillations caused by compressibility of the $\mathbf{E}\times\mathbf{B}$ drift velocity in the presence of the geodesic magnetic curvature and its characteristic frequency is roughly given by the ratio of the ion thermal velocity to the toroidal major radius. In this section (see also Appendix A for details), the poloidal- and toroidal-angle dependences of the GAM and its time evolution are mathematically analyzed by using Fourier and Laplace transform techniques and we obtain the dispersion relation, from which the real frequency and the damping rate of the GAM are derived. Since the characteristic parallel phase velocity of the GAM is on the order of the ion thermal velocity, particles resonant with the GAM are passing ions and thus effects of trapped ions are neglected here. We use Fourier and Laplace transforms with respect to (θ,ζ) and t, respectively, as

$$[\delta f^{(g)}_{\mathbf{k}_\perp}(\theta,\zeta,t),\phi_{\mathbf{k}_\perp}(\theta,\zeta,t)] = \sum_{l,m}\int\frac{d\omega}{2\pi}e^{il\theta-im\zeta-i\omega t}\times[\delta f_{k_r lm}(\omega),\phi_{k_r lm}(\omega)], \tag{12}$$

where $(v_\parallel,\mu)$ is used instead of (w,μ) as the independent velocity-space variables of $\delta f^{(g)}_{\mathbf{k}_\perp}$. The initial perturbed ion

gyrocenter distribution function is assumed to take the Maxwellian form $\delta f^{(g)}_{i\mathbf{k}_\perp}(t=0)=(\delta n^{(g)}_{i\mathbf{k}_\perp}(t=0)/n_0)F_{i0}$. Using the quasineutrality condition, the initial perturbed ion gyrocenter density is determined by $\delta n^{(g)}_{i\mathbf{k}_\perp}(t=0)=n_0(k_r^2a_i^2)(e\phi_{k_r00}(t=0)/T_i)$, with $a_i\equiv(T_i/m_i)^{1/2}/\Omega_i$. Here, $\phi_{k_rlm}(t=0)=0$ for $(l,m)\neq(0,0)$ and $k_r^2a_i^2\simeq\langle k_\perp^2a_i^2\rangle\ll 1$ are assumed. Then, as shown in Appendix A, $\phi_{k_r00}(\omega)$ is determined by

$$\frac{e\phi_{k_r00}(\omega)}{T_i}=\mathcal{K}_{\mathrm{GAM}}(\omega)\left[\frac{e\phi_{k_r00}(t=0)}{T_i}+\frac{\int d^3\boldsymbol{v}F_{i0}S_{ik_r00}(\omega)}{n_0(k_ra_i)^2}\right]. \tag{13}$$

Here, $\mathcal{K}_{\mathrm{GAM}}(\omega)$ is defined by

$$\frac{1}{\mathcal{K}_{\mathrm{GAM}}(\omega)}\equiv -i\hat{\omega}-i\frac{q^2}{2}\left[\left(\frac{R_0\epsilon_{10}}{r}\right)^2\{J(\hat{\omega})+J_{\mathrm{FOW}}(\hat{\omega})\}+L\left(\frac{R_0\epsilon_{L0}}{r}\right)^2J\left(\frac{\hat{\omega}}{L}\right)+\sum_{|n|\leqslant n_{\max}}\frac{(L+n)^2}{|L+n-qM|}\left(\frac{R_0\epsilon_h^{(n)}}{r}\right)^2\times J\left(\frac{\hat{\omega}}{|L+n-qM|}\right)\right], \tag{14}$$

with $\hat{\omega}\equiv R_0q\omega/v_{Ti}(v_{Ti}\equiv\sqrt{2T_i/m_i})$,

$$J(\hat{\omega})\equiv 2\hat{\omega}^3+3\hat{\omega}+(2\hat{\omega}^4+2\hat{\omega}^2+1)Z(\hat{\omega})-\frac{\hat{\omega}}{2}\{2\hat{\omega}+(2\hat{\omega}^2+1)Z(\hat{\omega})\}^2\left\{\frac{T_i}{T_e}+1+\hat{\omega}Z(\hat{\omega})\right\}^{-1}, \tag{15}$$

and

$$J_{\mathrm{FOW}}(\hat{\omega})\equiv i\frac{\sqrt{\pi}}{2}\left(\frac{k_rv_{Ti}q}{\Omega_i}\right)^2e^{-\hat{\omega}_r^2/4}\times\left\{\frac{\hat{\omega}_r^6}{64}+\left(\frac{\hat{\omega}_r^4}{8}+\frac{3\hat{\omega}_r^2}{4}+3+\frac{6}{\hat{\omega}_r^2}\right)\times\left(1-\frac{3\hat{\omega}_r}{16}\{2\hat{\omega}_r+(2\hat{\omega}_r^2+1)Z_r(\hat{\omega}_r)\}\times\left\{\frac{T_i}{T_e}+1+\hat{\omega}_rZ_r(\hat{\omega}_r)\right\}^{-1}\right)\right\}, \tag{16}$$

where $\hat{\omega}_r=\mathrm{Re}(\hat{\omega})$. On the right-hand side of Eq. (15), the plasma dispersion function $Z(\hat{\omega})\equiv\pi^{-1/2}\int_{-\infty}^{\infty}d\alpha e^{-\alpha^2}/(\alpha-\hat{\omega})$ is used. As explained in Appendix A, J_{FOW} given in Eq. (16) is derived from retaining the FOW effect on the $(l,m)=(\pm1,0)$ Fourier components of the gyrocenter distribution function. The dispersion relation, which determines the real frequency and the damping rate of the GAM oscillations, is given by $1/\mathcal{K}_{\mathrm{GAM}}(\omega)=0$ with Eq. (14). It is shown from Eq. (14) that, when $\epsilon_{L0}=\epsilon_h^{(n)}=0(|n|\leqslant n_{\max})$ and $J_{\mathrm{FOW}}=0$, our GAM dispersion relation coincides with the result of Lebedev *et al.* for the collisionless tokamak case. A rough approximation of the dispersion relation is given by $1/\mathcal{K}_{\mathrm{GAM}}(\omega)\simeq -i[\hat{\omega}-q^2(7/4+\tau_e)/\hat{\omega}]=0$, where $\epsilon_{10}=r/R_0$, $\epsilon_{L0}=0$, and $L\ll q\ll|L-qM|$ are assumed and $\tau_e\equiv T_e/T_i$ is used. Thus, in this simplest limit, the frequencies of the normal modes are written as $\hat{\omega}\equiv R_0q\omega/v_{Ti}\simeq\pm q(7/4+\tau_e)^{1/2}$ in which neither helical-ripple effects nor radial wave numbers are included. The zonal-flow electrostatic potential is expected to have largest amplitudes for these normal modes (or GAMs) except that the very-low-frequency potential (residual zonal flow), which is treated not in Sec. III but in Sec. IV, can also become large.

The inverse Laplace transform of Eq. (13) gives

$$\frac{e\phi_{k_r00}(t)}{T_i}=\mathcal{K}_{\mathrm{GAM}}(t)\frac{e\phi_{k_r00}(0)}{T_i}+\frac{1}{n_0(k_ra_i)^2}\times\int_0^t dt'\mathcal{K}_{\mathrm{GAM}}(t-t')\int d^3\boldsymbol{v}F_{i0}S_{ik_r00}(t'), \tag{17}$$

where $\mathcal{K}_{\mathrm{GAM}}(t)=(2\pi)^{-1}\int d\omega e^{-i\omega t}\mathcal{K}_{\mathrm{GAM}}(\omega)$ is the inverse Laplace transform of $\mathcal{K}_{\mathrm{GAM}}(\omega)$. Noting that $\delta f_{i\mathbf{k}_\perp}(t=0)=(k_r^2a_i^2)(e\phi_{k_r00}(t=0)/T_i)F_{i0}$ with $k_r^2a_i^2\ll 1$ is used and that electron contributions to the initial conditions and the source terms are neglected, we can verify that Eq. (17) takes the form of Eq. (11) with the replacement of the operator $N(t)\to\mathcal{K}_{\mathrm{GAM}}(t)\int d^3\boldsymbol{v}$. If we obtain the pair of solutions $\omega=\pm\omega_G+i\gamma$ to $1/K(\omega)=0$ which correspond to the minimum damping rate $-\gamma(>0)$, $\mathcal{K}_{\mathrm{GAM}}(t)$ is approximately written as

$$\mathcal{K}_{\mathrm{GAM}}(t)=\cos(\omega_Gt)\exp(\gamma t). \tag{18}$$

For the case, in which $L\ll\hat{\omega}_G\equiv R_0q\omega_G/v_{Ti}\ll|L-qM|$ and $\omega_G\gg|\gamma|$, approximate expressions for ω_G and γ are obtained as

$$\omega_G^2=\left(\frac{7+4\tau_e}{4}\right)q_*^2\left(\frac{v_{Ti}}{R_0q}\right)^2(1+L^2c_{L0}^2)\times\left[1+\frac{2(23+16\tau_e+4\tau_e^2)(1+L^4c_{L0}^2)}{q_*^2(7+4\tau_e)^2(1+L^2c_{L0}^2)^2}\right]\times\left[1+\frac{q_*^2}{2}\left(1+\frac{\pi\tau_e}{2(1+\tau_e)}\right)\sum_{|n|\leqslant n_{\max}}\frac{(L+n)^2(c_h^{(n)})^2}{(L+n-qM)^2}\right]^{-1}, \tag{19}$$

$$\gamma = -\frac{\sqrt{\pi}}{2} q_*^2 \left(\frac{v_{Ti}}{R_0 q}\right) \left[1 + \frac{2(23+16\tau_e+4\tau_e^2)(1+L^4 c_{L0}^2)}{q_*^2(7+4\tau_e)^2(1+L^2 c_{L0}^2)} + \frac{q_*^2}{2}\left(1+\frac{\pi\tau_e}{2(1+\tau_e)}\right) \sum_{|n|\le n_{\max}} \frac{(L+n)^2 (c_h^{(n)})^2}{(L+n-qM)^2} \right]^{-1}$$
$$\times \left[\exp(-\hat{\omega}_G^2)\{\hat{\omega}_G^4 + (1+2\tau_e)\hat{\omega}_G^2\} + \frac{1}{4}\left(\frac{k_r v_{Ti} q}{\Omega_i}\right)^2 \exp(-\hat{\omega}_G^2/4) \left\{ \frac{\hat{\omega}_G^6}{64} + \left(1+\frac{3}{8}\tau_e\right)\left(\frac{\hat{\omega}_G^4}{8}+\frac{3\hat{\omega}_G^2}{4}\right)\right\} \right.$$
$$\left. + \exp(-\hat{\omega}_G^2/L^2)(c_{L0}^2/L^3)\{\hat{\omega}_G^4 + (1+2\tau_e)L^2\hat{\omega}_G^2\} + \sum_{|n|\le n_{\max}} \frac{(L+n)^2 (c_h^{(n)})^2}{2|L+n-qM|} \left\{ 1 + \frac{\hat{\omega}_G^2}{(L+n-qM)^2}\left(1-\frac{\pi\tau_e^2}{2(1+\tau_e)^2}\right)\right\} \right], \tag{20}$$

where $\tau_e \equiv T_e/T_i$ and $q_* \equiv q(R_0\epsilon_{10}/r)$. Here, $q_*/q = R_0\epsilon_{10}/r$ is regarded as unity in conventional helical systems such as the LHD although q_*/q deviates from unity for some cases such as quasipoloidally symmetric systems[24] in which q_*/q approaches zero.

The dependence of the GAM frequency and damping rate on the Fourier spectrum of the magnetic-field strength in Eq. (1) is expressed in terms of $c_{L0} \equiv \epsilon_{L0}/\epsilon_{10}$ and $c_h^{(n)} \equiv \epsilon_h^{(n)}/\epsilon_{10}$ in Eqs. (19) and (20). The first line in Eq. (19) gives the lowest-order approximation of ω_G^2 and the square brackets below the first line show higher-order corrections. If we put $q_* \sim q \sim 1.5$, $T_e \sim T_i$, $L=2$, $M=10$, $\epsilon_{L0} \sim 0$, $\epsilon_h^{(0)} \sim \epsilon_{10}$, and $\epsilon_h^{(n)}=0$ for $n \neq 0$, the correction terms in the first and second brackets in Eq. (19) are roughly estimated as 0.3 and 0.05 where the latter smaller correction is due to helical ripples. We find that the same form of correction terms also appears in the first square bracket in the right-hand side of Eq. (20). The ϵ_{10} component in Eq. (1) produces the compressional fluctuation with the parallel wave number $1/(R_0 q)$ and causes the resonance of the GAM with passing ions at the parallel velocity $|v_\parallel| = R_0 q \omega_G$ which gives rise to the damping terms proportional to $\exp(-\hat{\omega}_G^2)$ in the second square bracket in the right-hand side of Eq. (20). The terms proportional to $(k_r v_{Ti} q/\Omega_i)^2 \exp(-\hat{\omega}_G^2/4)$ on the right-hand side of Eq. (20) are derived from J_{FOW} in Eq. (16) and represent the GAM damping due to the FOW effect. As explained in Ref. 13, since the FOW grows the fluctuation component with the poloidal wave number doubled, the parallel ion velocity required to resonate with the GAM is lowered to $|v_\parallel| = R_0 q \omega_G/2$ and the increased population of resonant ions enhances the GAM damping. Again, if we put $q_* \sim q \sim 1.5$, $T_e \sim T_i$, $L=2$, $M=10$, $\epsilon_{L0} \sim 0$, $\epsilon_h^{(0)} \sim \epsilon_{10}$, and $\epsilon_h^{(n)}=0$ for $n \neq 0$, the largest damping term in the second square bracket in Eq. (20) is the one due to the $(l,m)=(L,M)$ helical-ripple component $\epsilon_h^{(0)}$ in Eq. (1) and that is evaluated as ~ 0.15. For the (L,M) component, the resonance parallel velocity of the GAM becomes smaller than the thermal velocity so that ions with the resonance velocity are not only passing but also trapped. Thus, our approximation in Appendix A, where effects of trapped ions on the GAM damping are neglected, is not as accurate for the $(l,m)=(L,M)$ components as for the $(l,m)=(1,0)$ component. However, it is seen later from Figs. 3 and 4 that the resonance damping due to trapped ions is not so effective as due to the passing ions and therefore our analytical prediction of the GAM damping rate agrees with the simulation results fairly well.

We should recall that $\mathcal{K}_{\mathrm{GAM}}(\omega)$ given by Eq. (14) and its inverse Laplace transform $\mathcal{K}_{\mathrm{GAM}}(t)$ describe the short-time behavior of the zonal-flow potential, in which slow components with lower frequencies than the GAM frequency are dropped. The long-time behavior of the zonal-flow potential is investigated in the next section, where we find that an essential role is played by trapped particles which are ignored for investigating the GAM dynamics.

IV. COLLISIONLESS LONG-TIME BEHAVIOR OF ZONAL FLOWS

We here consider the long-time behavior of zonal flows, for which trapped particles need to be taken into account. The trapping parameter κ is defined by

$$\kappa^2 = \frac{1-\lambda B_0\{1-\epsilon_T(\theta)-\epsilon_H(\theta)\}}{2\lambda B_0 \epsilon_H(\theta)}, \tag{21}$$

where $\lambda \equiv \mu/w$. Then, particles trapped in helical ripples are characterized by $\kappa^2 < 1$. Using $l/(qM) \ll 1$, we approximate the field line element dl by $R_0 d\zeta$, where R_0 denotes the major radius of the toroid. Then, the orbital average within a helical ripple is defined by

$$\bar{A} = \begin{cases} \frac{1}{2}\Sigma_{\sigma=\pm 1} \int_{\zeta_1}^{\zeta_2} (R_0 d\zeta/|v_\parallel|) A \Big/ \int_{\zeta_1}^{\zeta_2} (R_0 d\zeta/|v_\parallel|) & \text{for } \kappa^2 < 1 \\ \int_{\zeta_0-\pi/M}^{\zeta_0+\pi/M} (R_0 d\zeta/|v_\parallel|) A \Big/ \int_{\zeta_0-\pi/M}^{\zeta_0+\pi/M} (R_0 d\zeta/|v_\parallel|) & \text{for } \kappa^2 > 1, \end{cases} \tag{22}$$

where $\sigma = v_\parallel/|v_\parallel|$ is the sign of the parallel velocity, (ζ_1, ζ_2) represents the toroidal-angle interval for a particle trapped within a helical ripple, and $(\zeta_0 - \pi/M, \zeta_0 + \pi/M)$ corresponds to a whole helical ripple around the local minimum of B at $\zeta = \zeta_0$.

Using the longitudinal adiabatic invariant J (Ref. 16) given by

$$J=\begin{cases} 2\displaystyle\int_{\zeta_1}^{\zeta_2} R_0 d\zeta |v_\parallel| & \text{for } \kappa^2<1 \\ \displaystyle\int_{\zeta_0-\pi/M}^{\zeta_0+\pi/M} R_0 d\zeta |v_\parallel| & \text{for } \kappa^2>1 \end{cases} = \begin{cases} 16(R_0/M)(\mu B_0 \epsilon_H/m)^{1/2}[E(\kappa)-(1-\kappa^2)K(\kappa)] & \text{for } \kappa^2<1 \\ 8(R_0/M)(\mu B_0\epsilon_H/m)^{1/2}\kappa E(\kappa^{-1}) & \text{for } \kappa^2>1 \end{cases} \tag{23}$$

and the time period τ_h by

$$\tau_h = m\frac{\partial J}{\partial w} = \begin{cases} 2\displaystyle\int_{\zeta_1}^{\zeta_2} R_0 d\zeta |v_\parallel| & \text{for } \kappa^2<1 \\ \displaystyle\int_{\zeta_0-\pi/M}^{\zeta_0+\pi/M} R_0 d\zeta |v_\parallel| & \text{for } \kappa^2>1 \end{cases} = \begin{cases} 4(R_0/M)(\mu B_0\epsilon_H/m)^{-1/2}K(\kappa) & \text{for } \kappa^2<1 \\ 2(R_0/M)(\mu B_0\epsilon_H/m)^{-1/2}\kappa^{-1}K(\kappa^{-1}) & \text{for } \kappa^2>1, \end{cases} \tag{24}$$

with the complete elliptic integrals $K(\kappa)$ and $E(\kappa)$, the orbital average of the radial drift velocity within a helical ripple is given by

$$\bar{v}_{dr} = \frac{mc}{e\psi'\tau_h}\frac{\partial J}{\partial\theta} = \begin{cases} \dfrac{c\mu B_0}{e\psi'}\left[\dfrac{\partial\epsilon_H}{\partial\theta}\left\{\dfrac{2E(\kappa)}{K(\kappa)}-1\right\}+\dfrac{\partial\epsilon_T}{\partial\theta}\right] & \text{for } \kappa^2<1 \\ \dfrac{c\mu B_0}{e\psi'}\left[\dfrac{\partial\epsilon_H}{\partial\theta}\left\{2\kappa^2\left(\dfrac{E(\kappa^{-1})}{K(\kappa^{-1})}-1\right)+1\right\}+\dfrac{\partial\epsilon_T}{\partial\theta}\right] & \text{for } \kappa^2>1, \end{cases} \tag{25}$$

where $\psi'=d\psi/dr$. The drift frequency ω_D is expressed as

$$\omega_D = k_r(\bar{v}_{dr}+v_\parallel \mathbf{b}\cdot\nabla\delta_r), \tag{26}$$

where $\delta_r=\int^l (dl/v_\parallel)(v_{dr}-\bar{v}_{dr})$ represents the radial displacement of the gyrocenter from the helical-ripple-averaged radial position. Then, Eq. (3) is rewritten as

$$\left(\frac{\partial}{\partial t}+v_\parallel\mathbf{b}\cdot\nabla+ik_r\bar{v}_{dr}\right)(g_{\mathbf{k}_\perp}e^{ik_r\delta_r}) = \frac{e}{T}F_0 e^{ik_r\delta_r}J_0\frac{\partial\phi_{\mathbf{k}_\perp}}{\partial t}+e^{ik_r\delta_r}S_{\mathbf{k}_\perp}F_0, \tag{27}$$

where we use (w,μ) [not $(v_\parallel,\mu)$ as in Sec. III] as the independent velocity-space variables.

Since the long-time behavior of zonal flows is considered, we regard Eq. (27) as already averaged in time over the time scale of the GAM oscillation period. Then, in Eq. (27), the time-derivative terms, the radial gyrocenter-drift term, and the source term are smaller than the parallel streaming term such that they are treated as of the higher order. The parallel derivative is rewritten as $\mathbf{b}\cdot\nabla\simeq R_0^{-1}(\partial/\partial\zeta+q^{-1}\partial/\partial\theta)$. Here, we also use $[\partial(g_{\mathbf{k}_\perp}e^{ik_r\delta_r})/\partial\theta]/[\partial(g_{\mathbf{k}_\perp}e^{ik_r\delta_r})/\partial\zeta]\sim r/R_0 \ll 1$. Based on these orderings, we expand $g_{\mathbf{k}_\perp}e^{ik_r\delta_r}$ as $g_{\mathbf{k}_\perp}e^{ik_r\delta_r}=h_0+h_1+\cdots$ and obtain the lowest-order equation $(v_\parallel/R_0)(\partial h_0/\partial\zeta)=0$ from Eq. (27). Thus, we can write $h_0=h_0(t,r,\theta,w,\mu,\sigma)$, where the dependence on $\sigma=v_\parallel/|v_\parallel|$ disappears for $\kappa^2<1$. The first-order equation is written as

$$\frac{v_\parallel}{R_0}\frac{\partial h_1}{\partial\zeta} = -\left(\frac{\partial}{\partial t}+\frac{v_\parallel}{R_0 q}\frac{\partial}{\partial\theta}+ik_r\bar{v}_{dr}\right)h_0+\frac{e}{T}F_0e^{ik_r\delta_r}J_0\frac{\partial\phi_{\mathbf{k}_\perp}}{\partial t} + e^{ik_r\delta_r}S_{\mathbf{k}_\perp}F_0. \tag{28}$$

As mentioned in Eqs. (10) and (11), the response of the zonal-flow potential to the nonlinear source terms can immediately be derived from the solution of the linear initial-value problem. Therefore, we hereafter ignore $S_{\mathbf{k}_\perp}$ until the response to the initial gyrocenter distribution is obtained.

For particles trapped in a helical ripple ($\kappa^2<1$), the orbital average of Eq. (28) and its time integration yield

$$\begin{aligned} h_0(t) &= h_0(0)e^{-ik_r\bar{v}_{dr}t}+\frac{e}{T}\int_0^t dt' e^{-ik_r\bar{v}_{dr}(t-t')}F_0 \times\overline{\left(e^{ik_r\delta_r}J_0\frac{\partial\phi_{\mathbf{k}_\perp}(t')}{\partial t'}\right)} \\ &= \overline{(e^{ik_r\delta_r}\delta f^{(g)}_{\mathbf{k}_\perp}(0))}e^{-ik_r\bar{v}_{dr}t}+\frac{e}{T}F_0\overline{(e^{ik_r\delta_r}J_0\phi_{\mathbf{k}_\perp}(t))} - ik_r\bar{v}_{dr}\frac{e}{T}\int_0^t dt' e^{-ik_r\bar{v}_{dr}(t-t')}F_0\overline{(e^{ik_r\delta_r}J_0\phi_{\mathbf{k}_\perp}(t'))}, \end{aligned} \tag{29}$$

where integration by parts and the lowest-order relation resulting from Eq. (5),

$$\overline{(e^{ik_r\delta_r}\delta f^{(g)}_{\mathbf{k}_\perp})} = -\frac{e}{T}F_0\overline{(e^{ik_r\delta_r}J_0\phi_{\mathbf{k}_\perp})}+h_0, \tag{30}$$

are used. We find from Eq. (29) that effects of $\bar{v}_{dr}$ on the distribution of helical-ripple-trapped particles strongly depend on time t. Here, we define a characteristic time τ_c by $\tau_c\sim 1/|k_r\bar{v}_{dr}|$ where $\bar{v}_{dr}$ is evaluated by considering typical helical-ripple-trapped particles. On the right-hand side of Eq. (29), for $t\ll\tau_c$, the third time-integral term can be neglected compared with the second term while, for $t\gg\tau_c$, the $0<t'<t-\tau_c$ part of the time-integral term makes a small contribution to the perturbed particle density because the phase mixing occurs in the velocity integration due to the factor $e^{-ik_r\bar{v}_{dr}(t-t')}$. Then, since we consider the long-time behavior

of the zonal-flow potential, we replace $\phi_{\mathbf{k}_\perp}(t')$ with $\phi_{\mathbf{k}_\perp}(t)$ in the time-integral term on the right-hand side of Eq. (29) and approximately obtain

$$h_0(t) \simeq \left[\overline{(e^{ik_r\delta_r}\delta f^{(g)}_{\mathbf{k}_\perp}(0))} + \frac{e}{T}F_0\overline{(e^{ik_r\delta_r}J_0\phi_{\mathbf{k}_\perp}(t))} \right] e^{-ik_r\bar{v}_{dr}t}, \tag{31}$$

which is shown to be valid for both short- and long-time limits.

When $\kappa^2 > 1$, using the periodic condition $h_1(\zeta + 2\pi/M) = h_1(\zeta)$ and taking the orbital average of Eq. (28) within a helical ripple give

$$\left(\frac{\partial}{\partial t} + \omega_\theta \frac{\partial}{\partial \theta} \right)(e^{ik_r\Delta_r}h_0) = \frac{e}{T}e^{ik_r\Delta_r}F_0\overline{\left(e^{ik_r\delta_r}J_0\frac{\partial \phi_{\mathbf{k}_\perp}}{\partial t} \right)}, \tag{32}$$

where

$$\omega_\theta = 2\pi\sigma/(qM\tau_h) \tag{33}$$

is the helical-ripple-averaged poloidal angular velocity and

$$\Delta_r = \sigma(qM/2\pi)(mc/e\psi')(J - J_t), \tag{34}$$

with J_t defined later represents the radial displacement of the helical-ripple-averaged gyrocenter position. For $\kappa^2 > 1$, particles are classified into two types, particles trapped by the toroidicity and passing particles. For these particles, we regard $\omega_\theta \partial(e^{ik_r\Delta_r}h_0)/\partial\theta$ as a dominant term in Eq. (32) based on the long-time ordering and expand $e^{ik_r\Delta_r}h_0$ as $e^{ik_r\Delta_r}h_0 = \eta_0 + \eta_1 + \cdots$, where η_0 is independent of θ because it satisfies the lowest-order equation $\omega_\theta \partial\eta_0/\partial\theta = 0$. The solubility condition for η_1 is derived from Eq. (32) and integrated in time to give

$$\begin{aligned} \eta_0(t) &= \eta_0(0) + \frac{e}{T}F_0\langle e^{ik_r\Delta_r}\overline{[e^{ik_r\delta_r}J_0\{\phi_{\mathbf{k}_\perp}(t) - \phi_{\mathbf{k}_\perp}(0)\}]}\rangle_{\mathrm{po}} \\ &= \langle e^{ik_r\Delta_r}\overline{(e^{ik_r\delta_r}\delta f^{(g)}_{\mathbf{k}_\perp}(0))}\rangle_{\mathrm{po}} \\ &\quad + \frac{e}{T}F_0\langle e^{ik_r\Delta_r}\overline{(e^{ik_r\delta_r}J_0\phi_{\mathbf{k}_\perp}(t))}\rangle_{\mathrm{po}}, \end{aligned} \tag{35}$$

where

$$\langle e^{ik_r\Delta_r}\overline{(e^{ik_r\delta_r}\delta f^{(g)}_{\mathbf{k}_\perp})}\rangle_{\mathrm{po}} = -\frac{e}{T}F_0\langle e^{ik_r\Delta_r}\overline{(e^{ik_r\delta_r}J_0\phi_{\mathbf{k}_\perp})}\rangle_{\mathrm{po}} + \eta_0 \tag{36}$$

is used and the poloidal-orbit average $\langle A\rangle_{\mathrm{po}}$ is defined by

$$\langle A\rangle_{\mathrm{po}} = \begin{cases} \dfrac{1}{2}\displaystyle\sum_{\sigma=\pm1}\int_{-\theta_t}^{\theta_t}(d\theta/|\omega_\theta|)A \Big/ \int_{-\theta_t}^{\theta_t}(d\theta/|\omega_\theta|) & \text{for toroidally trapped particles} \\ \displaystyle\int_0^{2\pi}(d\theta/|\omega_\theta|)A \Big/ \int_0^{2\pi}(d\theta/|\omega_\theta|) & \text{for passing particles.} \end{cases} \tag{37}$$

Here, θ_t is given by the condition $\kappa(\theta = \theta_t) = 1$ which is equivalent to $\omega_\theta(\theta = \theta_t) = 0$. Now, J_t is defined by $J_t = J(\theta = \theta_t)$ for toroidally trapped particles and by $J_t = J(\theta = \pi)$ for passing particles. It is noted that ϵ_H, κ, ω_θ, and J are all even functions of θ for the magnetic field given by Eq. (1).

On the lowest order of the long-time ordering, we substitute Eq. (31) into $g_{\mathbf{k}_\perp} = e^{-ik_r\delta_r}h_0$ for $\kappa^2 < 1$ and Eq. (35) into $g_{\mathbf{k}_\perp} = e^{-ik_r\delta_r}e^{-ik_r\Delta_r}\eta_0$ for $\kappa^2 > 1$ in order to evaluate the nonadiabatic parts of the density perturbations in Eq. (8). Consequently, the quasineutrality condition is rewritten as

$$\mathcal{L}(t)\phi_{\mathbf{k}_\perp}(t) = I(t), \tag{38}$$

where the operator $\mathcal{L}(t)$ is defined by

$$\begin{aligned} \mathcal{L}(t)\phi_{\mathbf{k}_\perp}(t) \equiv{}& n_0 e\left(\frac{1}{T_i} + \frac{1}{T_e} \right)\phi_{\mathbf{k}_\perp}(t) - \frac{e}{T_i}\int_{\kappa^2<1} d^3v F_{i0}J_0 e^{-ik_r\delta_r} \\ &\times \overline{(e^{ik_r\delta_r}J_0\phi_{\mathbf{k}_\perp}(t))}e^{-ik_r\bar{v}_{dri}t} - \frac{e}{T_i}\int_{\kappa^2>1} d^3v F_{i0} \times J_0 e^{-ik_r\delta_r}e^{-ik_r\Delta_r}\langle e^{ik_r\Delta_r}\overline{(e^{ik_r\delta_r}J_0\phi_{\mathbf{k}_\perp}(t))}\rangle_{\mathrm{po}} \\ &- \frac{e}{T_e}\int_{\kappa^2<1} d^3v F_{e0}\overline{\phi_{\mathbf{k}_\perp}(t)}e^{-ik_r\bar{v}_{dre}t} - \frac{e}{T_e}\int_{\kappa^2>1} d^3v F_{e0}\langle\overline{\phi_{\mathbf{k}_\perp}(t)}\rangle_{\mathrm{po}}, \end{aligned} \tag{39}$$

and $I(t)$ is written in terms of the initial gyrocenter distribution functions as

$$I(t) \equiv \int_{\kappa^2<1} d^3v J_0 e^{-ik_r\delta_r} e^{-ik_r\bar{v}_{dri}t} \overline{(e^{ik_r\delta_r}\delta f^{(g)}_{i\mathbf{k}_\perp}(0))} + \int_{\kappa^2>1} d^3v J_0 e^{-ik_r\delta_r} e^{-ik_r\Delta_r} \langle e^{ik_r\Delta_r} \overline{(e^{ik_r\delta_r}\delta f^{(g)}_{i\mathbf{k}_\perp}(0))}\rangle_{\mathrm{po}} - \int_{\kappa^2<1} d^3v e^{-ik_r\bar{v}_{dre}t} \overline{\delta f^{(g)}_{e\mathbf{k}_\perp}(0)} - \int_{\kappa^2>1} d^3v \langle \overline{\delta f^{(g)}_{e\mathbf{k}_\perp}(0)}\rangle_{\mathrm{po}}. \tag{40}$$

Now, we assume $k_\perp\rho$, $k_r\Delta_r$, ϵ_T, and ϵ_H to be small and use them as expansion parameters. We neglect $k_r\delta_r$ because generally δ_r is much smaller than ρ. In Eq. (40), we have already taken the small-electron-mass limit, in which $k_\perp\rho$, $k_r\delta_r$, $k_r\Delta_r \to 0$ for electrons. The initial source $I(t)$ is considered to be of order $k_\perp^2\rho^2$. Then, to the lowest order, Eq. (38) is written as $\mathcal{L}_0\phi_{\mathbf{k}_\perp}(t)=0$. Here and hereafter, we write the lowest-order potential by $\phi_{\mathbf{k}_\perp}(t)$ for simplicity. Defining the Hermitian inner product by

$$(u,v) \equiv \langle u^* v\rangle, \tag{41}$$

where $\langle\cdots\rangle$ denotes the flux-surface average, we obtain

$$(\phi_{\mathbf{k}_\perp}(t), \mathcal{L}_0\phi_{\mathbf{k}_\perp}(t)) = \sum_{a=e,i} \frac{e_a}{T_a} \left\langle \int d^3v F_{a0} |\phi_{\mathbf{k}_\perp}(t) - \overline{\phi_{\mathbf{k}_\perp}(t)}|^2 \right\rangle = 0. \tag{42}$$

From Eq. (42), we find that $\phi_{\mathbf{k}_\perp}(t) = \overline{\phi_{\mathbf{k}_\perp}(t)}$ and therefore $\phi_{\mathbf{k}_\perp}(t)$ is a flux-surface function, $\partial\phi_{\mathbf{k}_\perp}/\partial\zeta = \partial\phi_{\mathbf{k}_\perp}/\partial\theta = 0$, to the lowest order. From the next-order expression of Eq. (38), we have $(\phi_{\mathbf{k}_\perp}(t), \mathcal{L}_1(t)\phi_{\mathbf{k}_\perp}(t)) = (\phi_{\mathbf{k}_\perp}(t), I(t))$ which gives

$$\frac{e\phi_{\mathbf{k}_\perp}(t)}{T_i} = \frac{\langle I(t)\rangle}{\mathcal{D}(t)}, \tag{43}$$

where the shielding effects are represented by

$$\mathcal{D}(t) = \mathcal{D}_< + \mathcal{E}(t), \tag{44}$$

with

$$\mathcal{D}_< = \frac{1}{2}\left\langle \int d^3v F_{i0} k_\perp^2\rho^2 \right\rangle + \left\langle \int_{\kappa^2>1} d^3v F_{i0} k_r^2 \{\langle\Delta_r^2\rangle_{\mathrm{po}} - \langle\Delta_r\rangle_{\mathrm{po}}^2\} \right\rangle \tag{45}$$

and

$$\mathcal{E}(t) = \left\langle \int_{\kappa^2<1} d^3v F_{i0} J_0^2 (1 - e^{-ik_r\bar{v}_{dri}t}) \right\rangle + \frac{T_i}{T_e}\left\langle \int_{\kappa^2<1} d^3v F_{e0} (1 - e^{-ik_r\bar{v}_{dre}t}) \right\rangle. \tag{46}$$

On the right-hand side of Eq. (45), the first integral term represents the shielding effect of the classical ion polarization while the second integral terms correspond to the neoclassical polarization effect due to toroidally trapped ions ($\kappa^2>1$). We see from Eq. (46) that, for $t \ll \tau_c$, $\mathcal{E}(t)$ vanishes and thus $\mathcal{D}(t) \to \mathcal{D}_<$ while, for $t \gg \tau_c$, $\mathcal{E}(t)$ gives an additional shielding caused by the radial drift of nonadiabatic particles (both ions and electrons) trapped in helical ripples ($\kappa^2<1$). In the present work, as in the case of the ITG turbulence,[2] we neglect the electron source of the zonal-flow generation. Then, we also drop electron contributions to $\langle I(t)\rangle$ and write

$$\langle I(t)\rangle = \left\langle \int_{\kappa^2<1} d^3v e^{-ik_r\bar{v}_{dri}t} \overline{\delta f^{(g)}_{i\mathbf{k}_\perp}(0)} \right\rangle + \left\langle \int_{\kappa^2>1} d^3v e^{-ik_r\Delta_r} \langle e^{ik_r\Delta_r} \overline{\delta f^{(g)}_{i\mathbf{k}_\perp}(0)}\rangle_{\mathrm{po}} \right\rangle. \tag{47}$$

Using Eqs. (23)–(25), (33), (34), and (37), we rewrite Eqs. (45) and (46) as

$$\mathcal{D}_< = n_0\langle k_\perp^2 a_i^2\rangle(1+G) \tag{48}$$

and

$$\mathcal{E}(t) = \frac{2}{\pi} n_0 \left[\langle (2\epsilon_H)^{1/2}\{1 - g_{i1}(t,\theta)\}\rangle - \frac{3}{2}\langle k_\perp^2 a_i^2\rangle \times \langle (2\epsilon_H)^{1/2}\{1 - g_{i2}(t,\theta)\}\rangle + \frac{T_i}{T_e}\langle (2\epsilon_H)^{1/2}\{1 - g_{e1}(t,\theta)\}\rangle \right], \tag{49}$$

respectively. Here, the flux-surface average of functions of the poloidal angle θ is approximated by the poloidal-angle average, $\langle\cdots\rangle \simeq (2\pi)^{-1}\oint\cdots d\theta$. In Eq. (49), $g_{aj}(t,\theta)(a=i,e;j=1,2)$ are defined by

$$g_{aj}(t,\theta) = \int_0^1 d(\kappa^2)\frac{1}{2}K(\kappa)\frac{\cos\left[\left(j+\frac{1}{2}\right)\tan^{-1}(k_r V_{dra} t)\right]}{[1+(k_r V_{dra} t)^2]^{(j+1/2)/2}}, \tag{50}$$

where V_{dra} denotes the bounce-averaged radial drift velocity $\bar{v}_{dra}$ of helical-ripple-trapped particles evaluated at $v = v_{Ta} \equiv (2T_a/m_a)^{1/2}$ and is written as

$$V_{dra} = \frac{cT_a}{e\psi'}\left[\frac{\partial\epsilon_H}{\partial\theta}\left\{ 2\frac{E(\kappa)}{K(\kappa)} - 1 \right\} + \frac{\partial\epsilon_T}{\partial\theta} \right]. \tag{51}$$

The terms proportional to $\langle (2\epsilon_H)^{1/2} g_{aj}\rangle$ in Eq. (49) represent contributions from the nonadiabatic helical-ripple-trapped particles. When $t \ll \tau_c (\sim 1/|k_r V_{dra}|)$, $g_{aj} \simeq 1$. Then, the density perturbations of the nonadiabatic helical-ripple-trapped particles cancel those of the adiabatic helical-ripple-trapped particles and $\mathcal{E}(t)$ vanishes. On the other hand, when $t \gg \tau_c$, we see that $g_{aj} \simeq 0$. This implies that the density perturbations of the nonadiabatic helical-ripple-trapped particles are suppressed by the phase mixing associated with the helical-ripple-bounce-averaged radial drift so that $\mathcal{E}(t)$ becomes finite and positive, which causes the additional shielding of

the zonal-flow potential. Since not only ions but also electrons influence the quasineutrality condition through their bounce-averaged radial drift motions, $\mathcal{E}(t)$ in Eq. (49) shows the T_e dependence which becomes significant for $t \gg \tau_c$.

In Eq. (48), the geometrical factor G represents the ratio of the neoclassical polarization due to toroidally trapped ions to the classical polarization and is given by

$$G = \frac{12}{\pi^3} B_0 R_0^2 q^2 \left\langle \frac{B^2}{|\nabla\psi|^2} \right\rangle \left[\int_0^{1/B_M} d\lambda \oint \frac{d\theta}{2\pi} (2\lambda B_0 \epsilon_H)^{-1/2} \kappa^{-1} K(\kappa^{-1}) \right.$$
$$\times \left\{ (2\lambda B_0 \epsilon_H)^{1/2} \kappa E(\kappa^{-1}) - \frac{\oint (d\theta/2\pi) K(\kappa^{-1}) E(\kappa^{-1})}{\oint (d\theta/2\pi)(2\lambda B_0 \epsilon_H)^{-1/2} \kappa^{-1} K(\kappa^{-1})} \right\}^2$$
$$\left. + \int_{1/B_M}^{1/B'_m} d\lambda \int_{\kappa^2(\theta)>1} \frac{d\theta}{2\pi} (2\lambda B_0 \epsilon_H)^{1/2} \kappa K(\kappa^{-1}) \left\{ E(\kappa^{-1}) - \frac{1}{\kappa} \left(\frac{\epsilon_H(\theta_t)}{\epsilon_H} \right)^{1/2} \right\}^2 \right], \tag{52}$$

where B_M denotes the maximum field strength over the flux surface and B'_m represents the minimum value of local maximum field strengths within each helical ripple.

From Eqs. (43)–(48), we obtain

$$\frac{e\phi_{\mathbf{k}_\perp}(t)}{T_i} = \frac{1}{n_0 \langle k_\perp^2 a_i^2 \rangle} N(t)\, \delta f^{(g)}_{i\mathbf{k}_\perp}(0), \tag{53}$$

where the operator $N(t)$ is defined by

$$N(t)A \equiv [1 + G + \mathcal{E}(t)/(n_0 \langle k_\perp^2 a_i^2 \rangle)]^{-1} \left\langle \int_{\kappa^2<1} d^3\boldsymbol{v} e^{-ik_r \bar{v}_{dri} t} \bar{A} + \int_{\kappa^2>1} d^3\boldsymbol{v} e^{-ik_r \Delta_r} \langle e^{ik_r \Delta_r} \bar{A} \rangle_{\mathrm{po}} \right\rangle. \tag{54}$$

Here, G and $\mathcal{E}(t)$ are given by Eqs. (52) and (49), respectively, and A is an arbitrary gyrophase-independent phase-space function. Now that the response of the zonal-flow potential to the initial gyrocenter distribution is given by Eq. (53), we can immediately include the response to the $\mathbf{E}\times\mathbf{B}$ nonlinearity $F_{i0} S_{i\mathbf{k}_\perp}$ by using Eq. (11) and obtain the total zonal-flow potential as

$$\frac{e\phi_{\mathbf{k}_\perp}(t)}{T_i} = \frac{1}{n_0 \langle k_\perp^2 a_i^2 \rangle} \left[N(t)\, \delta f^{(g)}_{i\mathbf{k}_\perp}(0) + \int_0^t dt' N(t-t') F_{a0} S_{i\mathbf{k}_\perp}(t') \right], \tag{55}$$

where the electron source term is neglected.

Let us assume the initial perturbed ion gyrocenter distribution function to take the Maxwellian form $\delta f^{(g)}_{i\mathbf{k}_\perp}(0) \equiv -J_0(e\phi_{\mathbf{k}_\perp}(0)/T_i) F_{i0} + g_{i\mathbf{k}_\perp}(0) = (\delta n^{(g)}_{i\mathbf{k}_\perp}(0)/n_0) F_{i0}$. The quasineutrality condition gives $\delta n^{(g)}_{i\mathbf{k}_\perp}(0) = n_0 (k_\perp^2 a_i^2) \times (e\phi_{\mathbf{k}_\perp}(0)/T_i)$. Then, neglecting $\mathcal{O}(k_r^2 \Delta_r^2)$ terms in $e^{ik_r \Delta_r} = 1 + ik_r \Delta_r + \mathcal{O}(k_r^2 \Delta_r^2)$, Eq. (55) is rewritten as

$$\frac{e\phi_{\mathbf{k}_\perp}(t)}{T_i} = \mathcal{K}_L(t) \frac{e\phi_{\mathbf{k}_\perp}(0)}{T_i} + \frac{1}{n_0 \langle k_\perp^2 a_i^2 \rangle} \int_0^t dt' \mathcal{K}_L(t-t') \left\{ 1 - \frac{2}{\pi} \langle (2\epsilon_H)^{1/2} \{1 - g_{i1}(t-t', \theta)\} \rangle \right\}^{-1}$$
$$\times \left\langle \int_{\kappa^2<1} d^3\boldsymbol{v} e^{-ik_r \bar{v}_{dri}(t-t')} F_{i0} S_{i\mathbf{k}_\perp}(t') + \int_{\kappa^2>1} d^3\boldsymbol{v} F_{i0} S_{i\mathbf{k}_\perp}(t') \{1 + ik_r (\Delta_r - \langle \Delta_r \rangle_{\mathrm{po}})\} \right\rangle, \tag{56}$$

where

$$\mathcal{K}_L(t) \equiv \frac{1-(2/\pi)\langle(2\epsilon_H)^{1/2}\{1-g_{i1}(t,\theta)\}\rangle}{1+G+\mathcal{E}(t)/(n_0\langle k_\perp^2 a_i^2\rangle)}. \tag{57}$$

In contrast to $\mathcal{K}_{\rm GAM}(t)$ given by Eq. (18), the response kernel $\mathcal{K}_L(t)$ describes the the long-time behavior of the zonal-flow potential and takes the constant limiting values:

$$\mathcal{K}_< \equiv \lim_{t/\tau_c\to+0}\mathcal{K}_L(t) = \frac{1}{1+G} \tag{58}$$

and

$$\begin{aligned}\mathcal{K}_> \equiv \lim_{t/\tau_c\to+\infty}\mathcal{K}_L(t) &= \langle k_\perp^2 a_i^2\rangle[1-(2/\pi)\langle(2\epsilon_H)^{1/2}\rangle]\\ &\times\{\langle k_\perp^2 a_i^2\rangle[1-(3/\pi)\langle(2\epsilon_H)^{1/2}\rangle+G]\\ &+(2/\pi)(1+T_i/T_e)\langle(2\epsilon_H)^{1/2}\rangle\}^{-1}.\end{aligned} \tag{59}$$

Accordingly, we obtain

$$\frac{e\phi_{\mathbf{k}_\perp}(t)}{T_i} = \begin{cases} \mathcal{K}_<\left[\dfrac{e\phi_{\mathbf{k}_\perp}(0)}{T_i}+\dfrac{\displaystyle\int_0^t dt'\left\langle\int d^3\boldsymbol{v}F_{i0}S_{i\mathbf{k}_\perp}(t')\right\rangle}{n_0\langle k_\perp^2 a_i^2\rangle}\right] & \text{for } t\ll\tau_c \\ \mathcal{K}_>\left[\dfrac{e\phi_{\mathbf{k}_\perp}(0)}{T_i}+\dfrac{\displaystyle\int_0^t dt'\left\langle\int_{\kappa^2>1} d^3\boldsymbol{v}F_{i0}S_{i\mathbf{k}_\perp}(t')\right\rangle}{n_0\langle k_\perp^2 a_i^2\rangle\{1-(2/\pi)\langle(2\epsilon_H)^{1/2}\rangle\}}\right] & \text{for } t\gg\tau_c, \end{cases} \tag{60}$$

where $\mathcal{O}(k_r\Delta_r)$ terms are neglected.

The results shown in Eqs. (60) are the same as those derived in Ref. 3. The response kernel $\mathcal{K}_>$ for $t\gg\tau_c$ depends on T_e because $\mathcal{E}(t)$ in Eq. (49) does. The dependence of $\mathcal{K}_>$ on T_e and on the radial wave number shown in Eq. (59) is not seen in the tokamak case but appears here due to the radial drift of nonadiabatic helical-ripple-trapped particles whose population is proportional to $\epsilon_H^{1/2}$. In the axisymmetric limit $\epsilon_H\to+0$ with $\epsilon_T=\epsilon_t\cos\theta$ ($\epsilon_t\equiv r/R_0$), we obtain $G\to 1.6q^2/\epsilon_t^{1/2}$ and $\mathcal{K}_L(t)$ reduces to the Rosenbluth-Hinton[2] formula $\mathcal{K}_{\rm RH}=1/(1+1.6q^2/\epsilon_t^{1/2})$ for any time t. We should note that $k_\perp^2 a_i^2$ is a small parameter although it should be kept in Eqs. (57) and (59) to show the finiteness of the undamped (or residual) zonal flow and to derive the Rosenbluth-Hinton formula from these equations in the axisymmetric limit.

In the single-helicity case where $\epsilon_{L0}=0$ and $\epsilon_h^{(n)}=0$ for $n\neq 0$ [see Eq. (1)], $\epsilon_H=\epsilon_h^{(0)}$ is independent of θ and $\epsilon_T=(r/R_0)\cos\theta$. Then, Eqs. (25) and (51) reduce to $\bar{v}_{dra}=-(c\mu/e_aR_0)\sin\theta$ and $V_{dra}=-(cT_a/e_aR_0B_0)\sin\theta$, respectively. Accordingly, Eq. (50) is simplified as

$$g_{aj}(t,\theta) = \frac{\cos\left[\left(j+\frac{1}{2}\right)\tan^{-1}(k_rV_{dra}t)\right]}{[1+(k_rV_{dra}t)^2]^{(j+1/2)/2}} \quad (a=i,e;j=1,2) \tag{61}$$

and the characteristic time for the phase mixing due to the bounce-averaged radial drift is estimated as $\tau_c \simeq (k_rcT_i/eB_0R_0)^{-1}=(R_0/v_{ti})/(k_ra_i)$, where $a_i\simeq v_{ti}/\Omega_{i0}$, $\Omega_{i0}\equiv eB_0/(m_ic)$, and $v_{ti}\equiv v_{Ti}/\sqrt{2}\equiv(T_i/m_i)^{1/2}$ are used.

V. COMPLETE COLLISIONLESS TIME DEPENDENCE

Here, let us compare the expressions given by Eqs. (17) and (56) which represent the short- and long-time collisionless evolutions of the zonal-flow potential, respectively. These equations take similar forms to each other except that Eq. (56) contains additional terms resulting from radial drift motions of helical-ripple-trapped and toroidally trapped particles. Since only passing particles are considered in deriving Eq. (17), the short-time response kernel $\mathcal{K}_{\rm GAM}(t)$ vanishes in the long-time limit and it lacks the part of the residual zonal flow which is described by Eq. (56). We now present the complete collisionless time dependence of the zonal-flow potential by combining the short- and long-time expressions as

$$\begin{aligned}\frac{e\phi_{\mathbf{k}_\perp}(t)}{T_i} &= \mathcal{K}(t)\frac{e\phi_{\mathbf{k}_\perp}(0)}{T_i}+\frac{1}{n_0\langle k_\perp^2 a_i^2\rangle}\int_0^t dt'\mathcal{K}(t-t')\\ &\times\left\{1-\frac{2}{\pi}\langle(2\epsilon_H)^{1/2}\{1-g_{i1}(t-t',\theta)\}\rangle\right\}^{-1}\\ &\times\left\langle\int_{\kappa^2<1} d^3\boldsymbol{v}e^{-ik_r\bar{v}_{dri}(t-t')}F_{i0}S_{i\mathbf{k}_\perp}(t')\right.\\ &\left.+\int_{\kappa^2>1} d^3\boldsymbol{v}F_{i0}S_{i\mathbf{k}_\perp}(t')\{1+ik_r(\Delta_r-\langle\Delta_r\rangle_{\rm po})\}\right\rangle,\end{aligned} \tag{62}$$

where $\mathcal{K}(t)$ is defined in terms of $\mathcal{K}_{\rm GAM}(t)$ in Eq. (18) and $\mathcal{K}_L(t)$ in Eq. (57) as

$$\mathcal{K}(t) = \mathcal{K}_{\rm GAM}(t)[1-\mathcal{K}_L(t)]+\mathcal{K}_L(t). \tag{63}$$

The necessary conditions, $\mathcal{K}(t=0)=1$ and $\mathcal{K}(t)\to\mathcal{K}_L(t)$ as

$\mathcal{K}_{\mathrm{GAM}}(t)\to 0$, are satisfied by Eq. (63). Equation (63) represents that the GAM oscillations are superimposed around the averaged zonal-flow evolution expressed by $\mathcal{K}_L(t)$.

VI. NUMERICAL RESULTS

In order to examine the analytical results shown in the previous sections, a linearized ion gyrokinetic equation combined with the quasineutrality condition is numerically solved by a toroidal flux-tube gyrokinetic-Vlasov code.[6] The perturbed electron density is simply calculated by using $n_{e\mathbf{k}_\perp}=(n_0e/T_e)(\phi_{\mathbf{k}_\perp}-\langle\phi_{\mathbf{k}_\perp}\rangle)$ with $T_e=T_i$ in the present simulations and accordingly the radial drift motions of nonadiabatic helical-ripple-trapped electrons are not treated here. Thus, the terms proportional to T_i/T_e in Eqs. (49) and (59) should be dropped when comparing these formulas with the simulation results in this section. Here, we consider the $L=2/M=10$ single-helicity case, in which $\epsilon_h^{(n)}=0$ for $n\neq 0$ and therefore $\epsilon_H=\epsilon_h^{(0)}\equiv\epsilon_h$ is independent of θ. We also put $\epsilon_{10}=\epsilon_t=r/R_0$ and $\epsilon_{L0}=0$ so that $\epsilon_T=\epsilon_t\cos\theta$. The initial perturbed ion gyrocenter distribution function is given by the Maxwellian form $\delta f_{i\mathbf{k}_\perp}^{(g)}(0)=(\delta n_{i\mathbf{k}_\perp}^{(g)}(0)/n_0)F_{i0}$ with $\delta n_{i\mathbf{k}_\perp}^{(g)}(0)=n_0[1-\Gamma_0(b)](e\phi_{\mathbf{k}_\perp}(0)/T_i)$. We use $\bar{v}_{dr}=-(c\mu/eR_0)\sin\theta$, $k_\perp^2a_i^2\simeq k_r^2a_i^2$, and $\tau_c\simeq(k_rcT_i/eB_0R_0)^{-1}=(R_0/v_{ti})/(k_ra_i)$, where $a_i\simeq v_{ti}/\Omega_{i0}$, $\Omega_{i0}=eB_0/(m_ic)$, and $v_{ti}\equiv v_{Ti}/\sqrt{2}\equiv(T_i/m_i)^{1/2}$.

Time evolution of the zonal-flow potential obtained by the simulation is plotted by the solid circular symbols in Fig. 1(a) for the tokamak case ($\epsilon_h=0$) and in Fig. 1(b) for the helical system ($\epsilon_h=0.1$), respectively, where the unit of time is given by R_0/v_{ti}. In both cases, $q=1.5$ and $k_ra_i=0.131$ are used. In Figs. 1(a) and 1(b), the thick solid curves represent the response kernel $\mathcal{K}(t)$ obtained by Eq. (63) with the use of Eqs. (18) and (57) and the complex-valued GAM frequency $\omega=\omega_G+i\gamma$ calculated by numerically solving $1/\mathcal{K}_{\mathrm{GAM}}(\omega)=0$, where $\mathcal{K}_{\mathrm{GAM}}(\omega)$ is defined by Eq. (14). The numerical solution of $1/\mathcal{K}_{\mathrm{GAM}}(\omega)=0$ gives $(R_0\omega_G/v_{ti},R_0\gamma/v_{ti})=(2.774,-0.131)$ and $(2.711,-0.304)$ for the cases of Figs. 1(a) and 1(b), respectively, while Eqs. (19) and (20) give good approximations as $(R_0\omega_G/v_{ti},R_0\gamma/v_{ti})=(2.690,-0.139)$ and $(2.628,-0.365)$ for the same cases. Thus, the theoretical curves for $\mathcal{K}(t)$ in Figs. 1(a) and 1(b) do not change much when using these approximate values of (ω_G,γ). The thin solid curves in Figs. 1(a) and 1(b) represent the response kernel $\mathcal{K}(t)$ obtained by neglecting the FOW term J_{FOW} in Eq. (14) when calculating (ω_G,γ). Figure 1(a) shows a good agreement between the simulation result and the theoretical prediction with the FOW effect taken into account. For this case, without the FOW effect, the GAM damping rate is significantly underestimated. We see from Fig. 1(b) that, as theoretically predicted, the presence of helical ripples cause a significant enhancement of the GAM damping and a weak reduction of the GAM frequency. Compared with the case of Fig. 1(a), the theoretical curves for $\mathcal{K}(t)$ in Fig. 1(b) deviate from the simulation result toward the weaker damping of the GAM oscillations although the inclusion of the FOW effect gives a better approximation than in the no-FOW case. The deviation is anticipated to occur when ϵ_h, which is used like ϵ_t as a small parameter in our analytical treatment, increases.

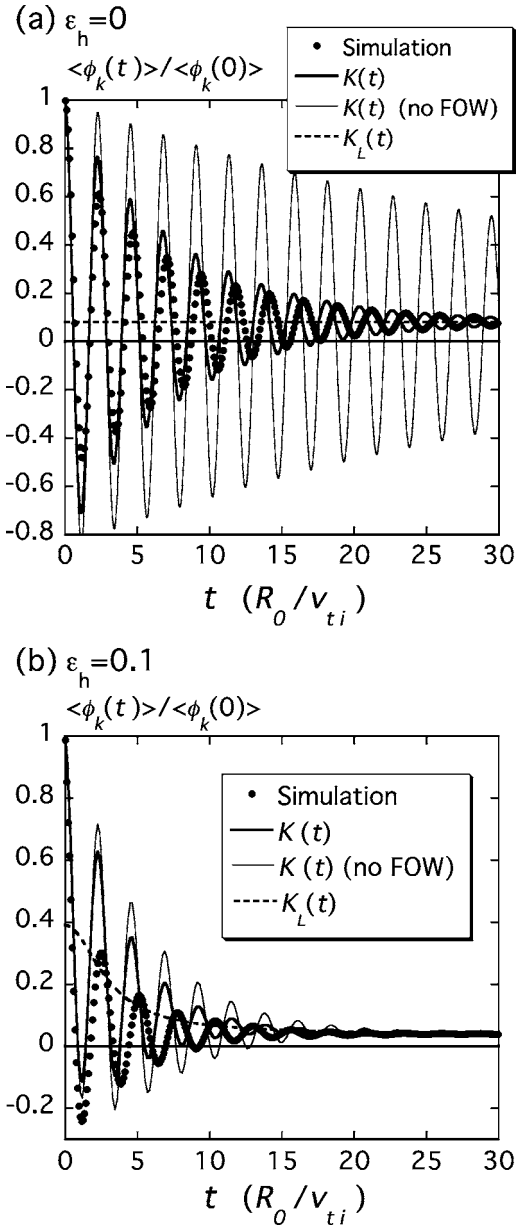

FIG. 1. Time evolution of the zonal-flow potential obtained by the simulations for the tokamak case ($\epsilon_h=0$) (a) and for the helical system ($\epsilon_h=0.1$) (b). In both case, $q=1.5$ and $k_ra_i=0.131$ are used. The simulation results are plotted by the solid circular symbols. The thick solid curves represent the response kernel $\mathcal{K}(t)$ obtained by Eq. (63) with the use of Eqs. (18) and (57) and the complex-valued GAM frequency $\omega=\omega_G+i\gamma$ calculated by numerically solving $1/\mathcal{K}_{\mathrm{GAM}}(\omega)=0$, where $\mathcal{K}_{\mathrm{GAM}}(\omega)$ is defined by Eq. (14). The thin solid curves represent the response kernel $\mathcal{K}(t)$ obtained by neglecting the FOW effect when calculating (ω_G,γ). The response kernel $\mathcal{K}_L(t)$ given by Eq. (57) is also plotted by the dashed lines.

The response kernel $\mathcal{K}_L(t)$ given by Eq. (57), which describes the long-time behavior of the zonal-flow potential with the GAM oscillations averaged out, is also plotted by the dashed lines in Figs. 1(a) and 1(b). [Note that, in Fig. 1(a) for the tokamak case, $\mathcal{K}_L(t)=\mathcal{K}_{\mathrm{R\text{-}H}}=1/(1+1.6q^2/\epsilon_t^{1/2})$ is given by a horizontal straight line.] For both cases, the simulation results show a convergence to $\mathcal{K}_L(t)$ in the long-time limit as theoretically predicted. At the early stage, the first undershooting of the simulation curve is shallower in Fig. 1(b) than in Fig. 1(a) even though the long-time limit $\mathcal{K}_>$

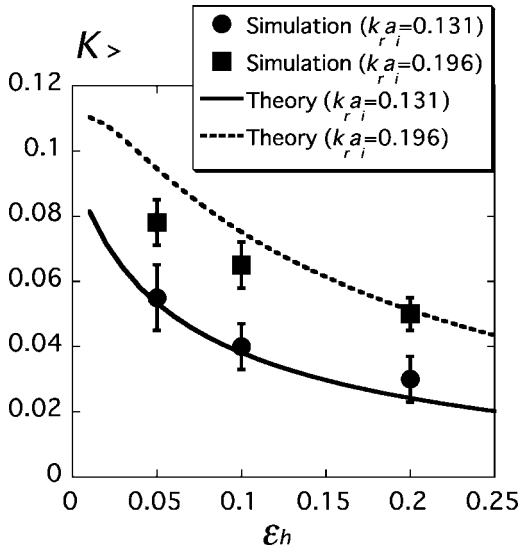

FIG. 2. The long-time limit of the response kernel $\mathcal{K}_>$ as a function of ϵ_h for $k_r a_i$=0.131, 0.196, and ϵ_t=0.1. The simulation results and the theoretical formula in Eq. (59) are represented by the symbols with error bars and curves, respectively.

$\equiv \lim_{t\to+\infty} \mathcal{K}_L(t)$=0.038 in the former case is smaller than $\mathcal{K}_{\rm RH}$=0.081 in the latter. This can be explained by our formula in Eq. (63) which predicts that the bottom of the early GAM oscillations is lifted with $\mathcal{K}_< \equiv \lim_{t\to+0} \mathcal{K}_L(t)$=0.39 for the helical system in Fig. 1(b). The theoretical estimation of the characteristic time $\tau_c \simeq (k_r c T_i/eB_0R_0)^{-1} = (R_0/v_{ti})/(k_r a_i)$ for $\mathcal{K}_L(t)$ to approach $\mathcal{K}_>$ in the single-helicity system gives $\tau_c \simeq 7.6(R_0/v_{ti})$ for Fig. 1(b). In Fig. 1(b), the GAM oscillations are not damped enough at $t<\tau_c$ to accurately identify $\mathcal{K}_L(t)$ from the simulation although an averaged behavior of the simulation curve over the oscillation period suggests a smaller value of τ_c than the theoretical prediction.

Figure 2 shows the long-time limit of the response kernel $\mathcal{K}_>$ as a function of ϵ_h for $k_r a_i$=0.131, 0.196, and ϵ_t=0.1. The simulation results and the theoretical formula in Eq. (59) are represented by the symbols with error bars and curves, respectively. The error bars occur due to the GAM oscillations which remain undamped in the final stage of the simulations. As seen from Eq. (20), the GAM damping becomes stronger with increasing ϵ_h and k_r. Also, τ_c is inversely proportional to k_r. Therefore, the evaluation of $\mathcal{K}_>$ for lower k_r requires longer-time collisionless gyrokinetic-Vlasov simulations using a larger number of grid points in the velocity space. In the present simulations, the velocity-space domain is bounded by $-5v_{ti} \leqslant v_\parallel \leqslant 5v_{ti}$ and $0 \leqslant v_\perp \equiv (2\mu B/m_i)^{1/2} \leqslant 5v_{ti}(B/B_0)^{1/2}$. The maximum numbers of grids used in the $v_\parallel$ and $v_\perp$ directions are $N_\parallel$=2048 and $N_\perp$=128, respectively. We find from Fig. 2 that the dependence of $\mathcal{K}_>$ on $(\epsilon_h, k_r a_i)$ obtained by the simulations is well predicted by the theoretical formula in Eq. (59). Since the parameters ϵ_h and $k_r a_i$ are assumed to be small in our theory, an excellent agreement between the simulation and the theory is confirmed in Fig. 2 for ϵ_h=0.05 and $k_r a_i$=0.131 which are both the smallest values used in the simulations here.

Figures 3(a) and 3(b) show the structures of the real part of the perturbed ion gyrocenter distribution function $\delta f^{(g)}_{i\mathbf{k}_\perp}$ on

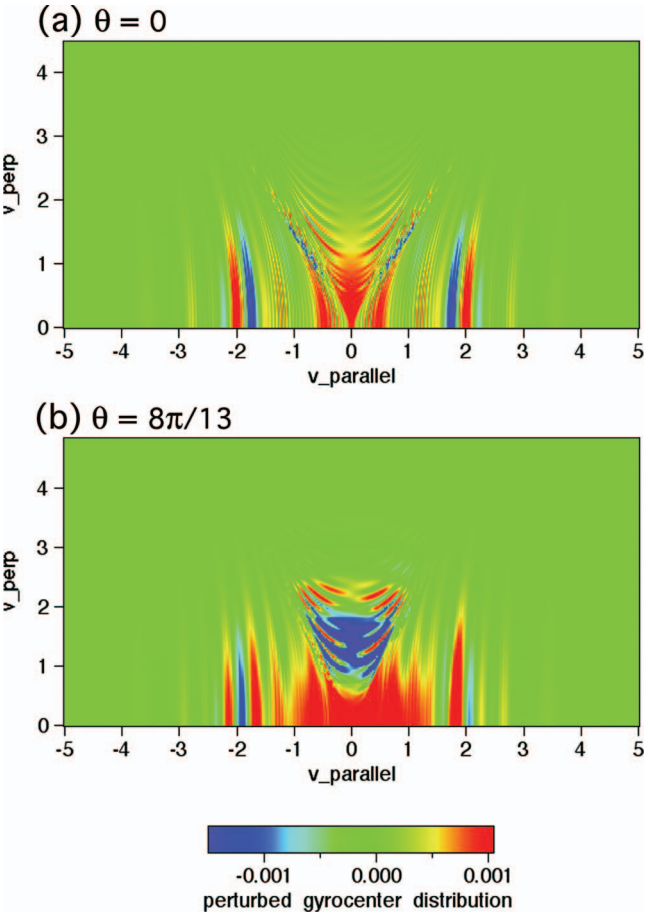

FIG. 3. (Color). Structures of the real part of the perturbed ion gyrocenter distribution function $\delta f^{(g)}_{i\mathbf{k}_\perp}$ on the $(v_\parallel, v_\perp)$ space obtained by the simulation at $t=12.5(R_0/v_{ti})$ for the case of the helical system in Fig. 1(b). The parallel and perpendicular velocities are both normalized by $v_{ti} \equiv (T_i/m_i)^{1/2}$. Here, (a) and (b) are plotted for $(\theta,\zeta)=(0,0)$ and $(\theta,\zeta)=(8\pi/13, 12\pi/13)$, respectively, in which the former corresponds to the the minimum of the magnetic-field strength within the flux surface and the latter locates the bottom of the local helical ripple with helical-ripple-trapped particles having relatively large radial drift velocities.

the $(v_\parallel, v_\perp)$ space obtained by the simulation at $t=12.5(R_0/v_{ti})$ for the case of the helical system in Fig. 1(b). Figures 3(a) and 3(b) are plotted for $(\theta,\zeta)=(0,0)$ and $(\theta,\zeta)=(8\pi/13, 12\pi/13)$, respectively. The poloidal and toroidal angles $(\theta,\zeta)=(0,0)$ used for Fig. 3(a) correspond to the minimum of the magnetic-field strength within the flux surface. There, the gyrocenter drift is tangential to the flux surface and the radial drift velocities of helical-ripple-trapped particles vanish. On the other hand, at $(\theta,\zeta)=(8\pi/13, 12\pi/13)$ for Fig. 3(b), the field strength is around the middle of its maximum and minimum due to the toroidal variation although the bottom of the local helical ripple is located there. For this case, helical-ripple-trapped particles have relatively large radial drift velocities. For comparison, the theoretical results corresponding to the simulation results in Figs. 3(a) and 3(b) are shown in Figs. 4(a) and 4(b), respectively, where the perturbed gyrocenter distribution function is analytically given from using Eqs. (31) and (35) as

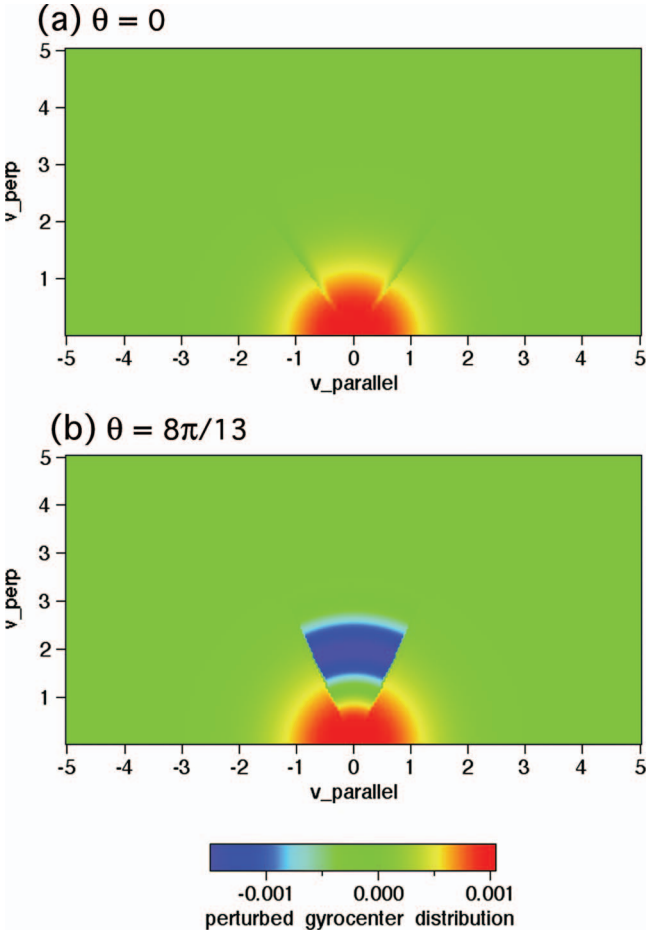

FIG. 4. (Color). Structures of the real part of the perturbed ion gyrocenter distribution function $\delta f_{i\mathbf{k}_\perp}^{(g)}$ on the $(v_\parallel, v_\perp)$ space obtained from the analytical solution given by Eqs. (64) and (65) at $t=12.5(R_0/v_{ti})$ for the case of the helical system in Fig. 1(b). Here, (a) and (b) correspond to the cases of Figs. 3(a) and 3(b), respectively.

$$\delta f_{i\mathbf{k}_\perp}^{(g)}(t) = \frac{e\phi_{\mathbf{k}_\perp}(0)}{T_i} F_{i0}\left[k_r^2 a_i^2 e^{-ik_r \bar{v}_{dr} t} - \mathcal{K}_L(t) \times \left(1 - \frac{1}{4}k_r^2\rho^2\right)\left(1 - e^{-ik_r\bar{v}_{dr}t}\right)\right] \quad \text{for } \kappa^2 < 1 \tag{64}$$

and

$$\delta f_{i\mathbf{k}_\perp}^{(g)}(t) = \frac{e\phi_{\mathbf{k}_\perp}(0)}{T_i} F_{i0}\left[k_r^2 a_i^2 - \mathcal{K}_L(t)\left\{ ik_r(\Delta_r - \langle\Delta_r\rangle_{\mathrm{po}}) + \frac{1}{2}k_r^2(\Delta_r - \langle\Delta_r\rangle_{\mathrm{po}})^2\right\}\right] \quad \text{for } \kappa^2 > 1. \tag{65}$$

Figures 3 and 4 plot the real part of $\delta f_{i\mathbf{k}_\perp}^{(g)}(t)$ normalized by $e\phi_{\mathbf{k}_\perp}(0)/T_i$.

The boundary between helically trapped and toroidally trapped regions is given by $\kappa=1$ [or $\lambda B_0(1-\epsilon_t\cos\theta+\epsilon_h)=1$], while the boundary between passing and toroidally trapped regions is given by $\lambda B_0(1+\epsilon_t+\epsilon_h)=1$ with $\lambda \equiv \mu/w \equiv (v_\perp/v)^2/B$. Then, we find that, for the case of Figs. 3(a) and 4(a), helically trapped, toroidally trapped, and passing regions are represented by $|v_\parallel/v_\perp|<0.5$, $0.5<|v_\parallel/v_\perp|<0.707$, and $0.707<|v_\parallel/v_\perp|$, respectively. In Figs. 3(a) and 4(a), the toroidally trapped region $0.5<|v_\parallel/v_\perp|<0.707$ is seen as two narrow oblique wedges just outside the fan-shaped helically trapped region $|v_\parallel/v_\perp|<0.5$. For the case of Figs. 3(b) and 4(b), helically trapped, toroidally trapped, and passing regions are represented by $|v_\parallel/v_\perp|<0.462$, $0.462<|v_\parallel/v_\perp|<0.532$, and $0.532<|v_\parallel/v_\perp|$, respectively. The toroidally trapped region $0.462<|v_\parallel/v_\perp|<0.532$ is so narrow that it is difficult to distinguish it from the other regions in Figs. 3(b) and 4(b).

Due to the parallel streaming of passing ions, stripes (or ballistic-mode structures) appear along the $v_\perp$ direction in the simulation results in Figs. 3(a) and 3(b). In this simulation, the parallel velocity for the resonance in Eq. (A13) is estimated as $v_\parallel = R_0 q\omega_G/2 \sim \pm 1.9 v_{ti}$, while the resonance due to helical ripples is expected to occur at $v_\parallel = R_0 q\omega_G/(L-qM) \sim \pm 0.3 v_{ti}$. Here, the GAM frequency ω_G observed from the laboratory frame is evaluated by $\omega_G = \pm 2\pi/T$, where $T \sim 2.5R_0/v_{ti}$ is used from the simulation result in Fig. 1(b). Actually, in Figs. 3(a) and 3(b), significantly deformed ion distributions are observed as prominent stripes around the above-mentioned resonance velocities in the passing region. These resonances contribute to collisionless damping of the GAM oscillations. The fine structures generated by the ballistic modes and the resonances in Figs. 3(a) and 3(b) are not seen in Figs. 4(a) and 4(b) because such rapid variations as the GAM oscillations are dropped from the analytical solutions in Eqs. (64) and (65) which are derived from taking the average along the rapid parallel motion to only include long-time behaviors as explained in Sec. IV.

At $\theta=0$, the radial drift velocity $\bar{v}_{dr}$ vanishes and Eq. (64) [or Fig. 4(a)] gives $\delta f_{i\mathbf{k}_\perp}^{(g)}(t) = (k_r^2 a_i^2)(e\phi_{\mathbf{k}_\perp}(0)/T_i)F_{i0}$ for helical-ripple-trapped ions [characterized by $\kappa^2 \equiv (2\epsilon_h)^{-1}\{1/(\lambda B_0) - 1 + \epsilon_t\cos\theta + \epsilon_h\} < 1$ with $\lambda \equiv (v_\perp/v)^2/B$] which remains unchanged from the initial distribution. On the other hand, Fig. 4(b) shows that, at $(\theta,\zeta) = (8\pi/13, 12\pi/13)$, the ion gyrocenter distribution in the helical-ripple-trapped region localized around $v_\parallel \sim 0$ has a distinctive hollow (a blue region) that is produced by a modulation along the $v_\perp$ direction due to the finite radial drift $\bar{v}_{dr}$. These characteristics predicted by the theoretical results in Figs. 4(a) and 4(b) are in a reasonable agreement with the average features of the corresponding distribution functions in Figs. 3(a) and 3(b) although some oscillatory structures caused by the ion parallel motion, which are averaged out in the former figures, are found in the latter figures even in the helical-ripple-trapped region. The resonance damping due to trapped ions does not seem to be so effective as due to the passing ions because deformation of the distribution functions in Fig. 3 from those in Fig. 4, which is caused by the GAM resonance, is not as evident in the trapped region as in the passing region even for the low parallel velocity $|v_\parallel| \sim R_0 q\omega_G/|L-qM| \sim 0.3 v_{ti}$. It is considered difficult for trapped ions, which repeat bounce motions, to keep the parallel velocity near the constant necessary for the resonance damping.

VII. CONCLUSIONS

In the present paper, collisionless short- and long-time behaviors of zonal flows in helical systems are theoretically investigated. A complete collisionless response of the zonal-flow potential to the initial potential and a given nonlinear source is derived in Eq. (62). The dispersion relation for the GAM oscillations, which occur in a short time scale, is analytically derived by taking account of the helical geometry and FOW orbits of passing ions. It is theoretically shown that the GAM frequency is slightly reduced by the helical ripples while the GAM damping rate is strongly enhanced by the ripples and the FOW effect. On the other hand, the collisionless long-time behavior of zonal flows in helical systems is influenced by the bounce-averaged radial drift motions of helical-ripple-trapped particles. It is predicted that, under the influence of helical-ripple-trapped particles, for the lower radial wave numbers, the long-time limit of the zonal-flow potential amplitude (or the residual flow) becomes smaller although simultaneously the characteristic transition time $\tau_c(\sim 1/k_r|\bar{v}_{dr}|)$ becomes longer. The validity of our analytical results on the zonal-flow evolution and on the velocity-space structures of the ion gyrocenter distribution is verified by the gyrokinetic-Vlasov simulations for the helical geometries with the single helicity.

In this work, collisional effects are neglected. Collisional decay of zonal flows is anticipated to occur in the long course of time although the residual zonal flows in a collisionless time scale still influence the turbulent transport. In some optimized helical configurations such as quasipoloidally symmetric systems[24] which significantly reduce neoclassical transport by suppressing both $|\bar{v}_{dr}|$ and G, we expect the response kernels $\mathcal{K}_>$, $\mathcal{K}_<$, and τ_c to increase such that large zonal flows can be maintained for a long-time period and contribute to a reduction of anomalous transport as well. More detailed simulation studies of the multihelicity systems including collisions remain as interesting future problems to investigate the control of the GAM oscillations and the residual zonal flows.

ACKNOWLEDGMENTS

The authors thank Dr. S. Satake for useful discussions on zonal-flow simulations.

This work is supported in part by the Ministry of Education, Culture, Sports, Science and Technology of Japan, Grant Nos. 16560727 and 17360445 and in part by the NIFS Collaborative Research Program, NIFS04KDAD003, NIFS04KNXN023, and NIFS04KLDD003.

APPENDIX: DERIVATION OF EQUATION (13)

In this appendix, we see how Eq. (13) is derived. Here, we use $(v_\parallel, \mu)$ instead of (w, μ) as the independent velocity-space variables of the the gyrocenter distribution function. Then, $v_\parallel \mathbf{b}\cdot\nabla$ in Eqs. (3) and (7) should be replaced with $v_\parallel \mathbf{b}\cdot\nabla - (\mu/m)(\mathbf{b}\cdot\nabla B)\partial/\partial v_\parallel$, where the last term represents the effect of the mirror force. Since the characteristic parallel phase velocity of the GAM is on the order of the ion thermal velocity, particles resonant with the GAM are not trapped but passing ions. Thus, we now consider only passing ions, for which we neglect the mirror-force term and rewrite Eq. (7) as

$$\left[\frac{\partial}{\partial t} + \frac{v_\parallel}{R_0}\left(\frac{\partial}{\partial \zeta} + \frac{1}{q}\frac{\partial}{\partial \theta}\right)\right](e^{ik_r d_r}\delta\hat{f}^{(g)}_{\mathbf{k}_\perp}) = -\frac{v_\parallel}{R_0}\left(\frac{\partial}{\partial \zeta} + \frac{1}{q}\frac{\partial}{\partial \theta}\right)\left(e^{ik_r d_r} J_0 \frac{e\phi_{\mathbf{k}_\perp}}{T}\right) + e^{ik_r d_r} S_{\mathbf{k}_\perp}, \tag{A1}$$

where $\delta\hat{f}^{(g)}_{\mathbf{k}_\perp} \equiv \delta f^{(g)}_{\mathbf{k}_\perp}/F_0$, $\omega_D = v_\parallel \mathbf{b}\cdot\nabla(k_r d_r) = -ie^{-ik_r d_r} v_\parallel \mathbf{b}\cdot\nabla e^{ik_r d_r}$, and $\mathbf{b}\cdot\nabla \simeq R_0^{-1}(\partial/\partial\zeta + q^{-1}\partial/\partial\theta)$ are used. Here, the radial displacement d_r of the passing ion from the orbit-averaged radial position is given by

$$d_r \equiv \hat{\delta}_{10}\cos\theta + \hat{\delta}_{L0}\cos(L\theta) + \sum_{|n|\le n_{\max}} \hat{\delta}_{L+n,M}\cos\{(L+n)\theta - M\zeta\}, \tag{A2}$$

where

$$\hat{\delta}_{10} = (R_0 q/r\Omega)\epsilon_{10}(v_\parallel + v_\perp^2/2v_\parallel),$$

$$\hat{\delta}_{L0} = (R_0 q/r\Omega)\epsilon_{L0}(v_\parallel + v_\perp^2/2v_\parallel), \tag{A3}$$

$$\hat{\delta}_{L+n,M} = (R_0 q/r\Omega)\epsilon_h^{(n)}(v_\parallel + v_\perp^2/2v_\parallel) \times (L+n)/[(L+n) - qM].$$

Recall that $(v_\parallel, \mu)$ are used as the independent velocity-space variables in Eq. (A1) where the mirror-force term is neglected. Using Fourier and Laplace transforms as shown in Eq. (12), Eq. (A1) is solved with the aid of the formula $e^{ix\cos y} = \Sigma_n i^n J_n(x) e^{iny}$ (J_n: the nth-order Bessel function) to yield

$$\delta\hat{f}_{k_r lm}(\omega) = \sum_{n_{10}, n'_{10}} i^{n'_{10}-n_{10}} J_{n_{10}}(k_r\hat{\delta}_{10}) J_{n'_{10}}(k_r\hat{\delta}_{10}) \sum_{n_{L0}, n'_{L0}} i^{n'_{L0}-n_{L0}} J_{n_{L0}}(k_r\hat{\delta}_{L0}) J_{n'_{L0}}(k_r\hat{\delta}_{L0}) \times \prod_{|n|\le n_{\max}} \left(\sum_{n_{L+n,M}, n'_{L+n,M}} i^{n'_{L+n,M}-n_{L+n,M}} J_{n_{L+n,M}}(k_r\hat{\delta}_{L+n,M}) J_{n'_{L+n,M}}(k_r\hat{\delta}_{L+n,M}) \right) \times \left(\frac{(l - qm + \lambda - q\mu)(v_\parallel/R_0 q)}{\omega - (l - qm + \lambda - q\mu)(v_\parallel/R_0 q)} \right) \frac{e}{T}\phi_{k_r, l+\lambda-\lambda', m+\mu-\mu'}(\omega) + \delta\hat{I}_{k_r lm}(\omega), \tag{A4}$$

for $(l,m) \neq (0,0)$ Fourier components, where $\delta\hat{f}_{k_r lm} \equiv \delta f_{k_r lm}/F_0$. [We should note that, for $(l,m) = (0,0)$, the parallel streaming

term vanishes and the neglect of the mirror-force term in Eq. (A1) is not a good approximation.] On the right-hand side of Eq. (A4),

$$\lambda \equiv n_{10} + L n_{L0} + \sum_{|n| \leqslant n_{\max}} (L+n) n_{L+n,m},$$

$$\lambda' \equiv n'_{10} + L n'_{L0} + \sum_{|n| \leqslant n_{\max}} (L+n) n'_{L+n,m},$$

$$\mu \equiv M \sum_{|n| \leqslant n_{\max}} n_{L+n,M}, \tag{A5}$$

$$\mu' \equiv M \sum_{|n| \leqslant n_{\max}} n'_{L+n,M}.$$

are used and the zero-gyroradius limit $k_r \rho \to +0$ [or $J_0(k_r\rho) \to 1$], which is uninfluential to the GAM damping, is taken. The initial conditions and the nonlinear source are included on the right-hand side of Eq. (A4) through

$$\begin{aligned}\delta\hat{I}_{k_r lm}(\omega) = i \sum_{n_{10}, n'_{10}} i^{n'_{10}-n_{10}} J_{n_{10}}(k_r \hat{\delta}_{10}) J_{n'_{10}}(k_r \hat{\delta}_{10}) \sum_{n_{L0}, n'_{L0}} i^{n'_{L0}-n_{L0}} J_{n_{L0}}(k_r \hat{\delta}_{L0}) J_{n'_{L0}}(k_r \hat{\delta}_{L0}) \\ \times \prod_{|n| \leqslant n_{\max}} \left(\sum_{n_{L+n,M}, n'_{L+n,M}} i^{n'_{L+n,M}-n_{L+n,M}} J_{n_{L+n,M}}(k_r \hat{\delta}_{L+n,M}) J_{n'_{L+n,M}}(k_r \hat{\delta}_{L+n,M}) \right) [\omega - (l - qm + \lambda - q\mu)(v_\parallel / R_0 q)]^{-1} \\ \times [\delta\hat{f}_{k_r, l+\lambda-\lambda', m+\mu-\mu'}(t=0) + S_{k_r, l+\lambda-\lambda', m+\mu-\mu'}(\omega)].\end{aligned} \tag{A6}$$

We find from Eqs. (A4) and (A6) that, even for the single (l,m) Fourier component, the multiple resonance conditions $\omega - (l - qm + \lambda - q\mu)(v_\parallel / R_0 q) = 0$ appear according to various numbers of (λ, μ). Without finite orbit widths (FOWs), the resonance conditions, in which $\lambda \neq 0$ or $\mu \neq 0$, never appear. The FOW effects given by the $(\lambda, \mu) \neq (0,0)$ terms may seem to be weak for longer radial wavelengths than the orbit widths since small non-zeroth-order Bessel function factors and couplings to small potential components with higher Fourier-mode numbers appear as seen in Eqs. (A4) and (A6). However, as shown in Ref. 13, the FOW effect on the GAM damping is significant for the $(l,m) = (\pm 1, 0)$ Fourier components which correspond to the longest parallel wavelength $(= 2\pi R_0 q)$. This is because, without the FOW, the population of ions with the highest resonant parallel velocity $(|v_\parallel| = R_0 q \omega)$ can be negligibly small while, with the FOW, the lower resonant velocity $(|v_\parallel| = R_0 q \omega / 2)$ and accordingly the larger population of resonant ions are produced [see that the resonance condition $\omega = \pm 2(v_\parallel / R_0 q)$ appears in Eq. (A4) for $l = \lambda = n_{10} = \pm 1$, $m = \mu = 0$, and $n_{L0} = n_{L+n,M} = 0$ $(|n| \leqslant n_{\max})$]. Thus, we retain this FOW effect on the $(l,m) = (\pm 1, 0)$ components $\delta\hat{f}_{ik_r \pm 10}$ in the following analysis of the GAM. For other Fourier components with $(l,m) \neq (\pm 1, 0)$, the FOW effects are relatively small and we neglect them by retaining only the terms with $n_{10} = n_{L0} = n_{L+n,M} = 0$ $(|n| \leqslant n_{\max})$ in Eqs. (A4) and (A6), for which $(\lambda, \mu) = (0,0)$ [but $(\lambda', \mu') \neq (0,0)$ for some of these terms].

Using Eq. (9), we obtain

$$\int d^3 v F_{i0} \delta\hat{f}_{ik_r lm} - n_0 (k_r a_i)^2 \frac{e\phi_{k_r lm}}{T_i} = \delta n_{ek_r lm}, \tag{A7}$$

where $1 - \Gamma_0(b) \simeq b$ [for $b = (k_\perp a_i)^2 \ll 1$], $a_i \equiv (T_i / m_i)^{1/2} / \Omega_i$, and $k_\perp \simeq k_r$ are used and subscripts referring to particle species are explicitly shown. The second term on the left-hand side of Eq. (A7) represents the ion polarization. For $(l,m) \neq (0,0)$ modes, the perturbed electron density is approximately given by the Boltzmann relation, $n_{ek_r lm} = n_0 e\phi_{k_r lm} / T_e$, because of the fast parallel motions of electrons. Then, Eq. (A7) is rewritten as

$$\int d^3 v F_{i0} \delta\hat{f}_{ik_r lm}(\omega) = n_0 \frac{e\phi_{k_r lm}(\omega)}{T_e} \quad \text{for } (l,m) \neq (0,0), \tag{A8}$$

where $k_r a_i \ll 1$ is used. Taking the time differentiation and the flux-surface average of Eq. (9) and using Eq. (7), we obtain

$$n_0(k_\perp a_i)^2\frac{e}{T_i}[-i\omega\phi_{k_r00}(\omega)-\phi_{k_r00}(t=0)]=\int d^3v F_{i0}\frac{k_r}{2r\Omega_i}\left(v_\parallel^2+\frac{\mu B_0}{m_i}\right)\Bigg[\epsilon_{10}\left\{\delta\hat{f}_{ik_r-10}(\omega)+\frac{e\phi_{k_r-10}(\omega)}{T_i}-\delta\hat{f}_{ik_r10}(\omega)-\frac{e\phi_{k_r10}(\omega)}{T_i}\right\}$$
$$+L\epsilon_{L0}\left\{\delta\hat{f}_{ik_r-L0}(\omega)+\frac{e\phi_{k_r-L0}(\omega)}{T_i}-\delta\hat{f}_{ik_rL0}(\omega)-\frac{e\phi_{k_rL0}(\omega)}{T_i}\right\}+\sum_{|n|\leqslant n_{\max}}L\epsilon_h^{(n)}$$
$$\times\left\{\delta\hat{f}_{ik_r,-L-n,-M}(\omega)+\frac{e\phi_{k_r,-L-n,-M}(\omega)}{T_i}-\delta\hat{f}_{ik_r,L+n,M}(\omega)-\frac{e\phi_{k_r,L+n,M}(\omega)}{T_i}\right\}\Bigg]$$
$$+\int d^3v F_{i0}S_{ik_r00}(\omega), \tag{A9}$$

where the flux-surface average is approximately given by the poloidal- and toroidal-angle averages, $\oint(d\theta/2\pi)\oint(d\zeta/2\pi)\cdots$. Electron contributions do not appear in Eq. (A9) because $\delta\hat{f}_{ek_rlm}=(e\phi_{k_rlm}/T_e)F_{e0}$ is used for $(l,m)\neq(0,0)$.

Neglecting terms of the second and higher orders in the radial wave number except for influential FOW terms, we obtain from Eq. (A4)

$$\delta\hat{f}_{ik_r10}(\omega)=\left[\frac{(v_\parallel/R_0q)}{\omega-(v_\parallel/R_0q)}+\frac{2(v_\parallel/R_0q)}{\omega-2(v_\parallel/R_0q)}\left(\frac{k_r\hat{\delta}_{10}}{2}\right)^2\right]$$
$$\times\left[\frac{e\phi_{k_r10}(\omega)}{T_i}+i\frac{e\phi_{k_r00}(\omega)}{T_i}\left(\frac{k_r\hat{\delta}_{10}}{2}\right)\right]$$
$$+\delta\hat{I}_{ik_r10}(\omega), \tag{A10}$$

$$\delta\hat{f}_{ik_rL0}(\omega)=\frac{L(v_\parallel/R_0q)}{\omega-L(v_\parallel/R_0q)}\left[\frac{e\phi_{k_rL0}(\omega)}{T_i}+i\frac{e\phi_{k_r00}(\omega)}{T_i}\right.$$
$$\left.\times\left(\frac{k_r\hat{\delta}_{L0}}{2}\right)\right]+\delta\hat{I}_{ik_rL0}(\omega), \tag{A11}$$

and

$$\delta\hat{f}_{ik_r,L+n,M}(\omega)=\frac{(L+n-qM)(v_\parallel/R_0q)}{\omega-(L+n-qM)(v_\parallel/R_0q)}$$
$$\times\left[\frac{e\phi_{k_r,L+n,M}(\omega)}{T_i}\right.$$
$$\left.+i\frac{e\phi_{k_r00}(\omega)}{T_i}\left(\frac{k_r\hat{\delta}_{L+n,M}}{2}\right)\right]$$
$$+\delta\hat{I}_{ik_r,L+n,M}(\omega). \tag{A12}$$

On the right-hand side of Eq. (A10), we see two resonance conditions $\omega=v_\parallel/R_0q$ and $\omega=2v_\parallel/R_0q$. The latter is induced by the FOW and it can significantly affect the damping of the GAM oscillations as remarked after Eq. (A6). On the other hand, the FOW effect on the real frequency of the GAM is weak because of the small factor $(k_r\hat{\delta}_{10}/2)^2$ appearing together with the factor $1/[\omega-2(v_\parallel/R_0q)]$. Then, in Eq. (A10), we retain the resonant (or imaginary) part of $1/[\omega-2(v_\parallel/R_0q)]$ while neglecting its nonresonant (or real) part. Thus, when using Eq. (A10) for evaluations of velocity-space integrals, we perform the replacement,

$$1/[\omega-2(v_\parallel/R_0q)]\rightarrow-i\pi\delta[\omega_r-2(v_\parallel/R_0q)], \tag{A13}$$

where $|\omega_i/\omega_r|\ll1$ with $(\omega_r,\omega_i)\equiv(\mathrm{Re}(\omega),\mathrm{Im}(\omega))$ is assumed.

Substituting Eqs. (A10)–(A12) into Eq. (A8), we obtain

$$\frac{e\phi_{k_r10}(\omega)}{T_i}=\left\{\frac{T_i}{T_e}+1+\hat{\omega}Z(\hat{\omega})\right\}^{-1}\Bigg[\left(-i\frac{k_rv_{Ti}}{4\Omega_i}\frac{R_0q}{r}\right)$$
$$\times\Bigg\{[2\hat{\omega}+(2\hat{\omega}^2+1)Z(\hat{\omega})]+i\sqrt{\pi}\left(\frac{k_rv_{Ti}q}{\Omega_i}\right)^2$$
$$\times e^{-\hat{\omega}_r^2/4}\left(\frac{\hat{\omega}_r^4}{32}+\frac{3\hat{\omega}_r^2}{16}+\frac{3}{4}+\frac{3}{2\hat{\omega}_r^2}\right)\Bigg\}$$
$$\times\epsilon_{10}\frac{e\phi_{k_r00}(\omega)}{T_i}+\int d^3v\frac{F_{i0}}{n_0}\delta\hat{I}_{ik_r10}(\omega)\Bigg], \tag{A14}$$

$$\frac{e\phi_{k_rL0}(\omega)}{T_i}=\left\{\frac{T_i}{T_e}+1+\frac{\hat{\omega}}{L}Z\left(\frac{\hat{\omega}}{L}\right)\right\}^{-1}$$
$$\times\Bigg[\left\{2\frac{\hat{\omega}}{L}+\left(2\left(\frac{\hat{\omega}}{L}\right)^2+1\right)Z\left(\frac{\hat{\omega}}{L}\right)\right\}$$
$$\times\left(-i\frac{k_rv_{Ti}}{4\Omega_i}\frac{R_0q}{r}\right)\epsilon_{L0}\frac{e\phi_{k_r00}(\omega)}{T_i}$$
$$+\int d^3v\frac{F_{i0}}{n_0}\delta\hat{I}_{ik_rL0}(\omega)\Bigg], \tag{A15}$$

and

$$\frac{e\phi_{k_r,L+n,M}(\omega)}{T_i}=\left\{\frac{T_i}{T_e}+1+\frac{\hat{\omega}}{|L+n-qM|}Z\left(\frac{\hat{\omega}}{|L+n-qM|}\right)\right\}^{-1}\left[\left\{2\frac{\hat{\omega}}{|L+n-qM|}+\left(2\left(\frac{\hat{\omega}}{|L+n-qM|}\right)^2+1\right)\right.\right.$$
$$\left.\left.\times Z\left(\frac{\hat{\omega}}{|L+n-qM|}\right)\right\}\left(-i\frac{k_r\upsilon_{Ti}}{4\Omega_i}\frac{R_0q}{r}\right)\left(\frac{(L+n)\epsilon_h^{(n)}}{|L+n-qM|}\right)\frac{e\phi_{k_r00}(\omega)}{T_i}+\int d^3\upsilon\frac{F_{i0}}{n_0}\delta\hat{I}_{ik_r,L+n,M}(\omega)\right], \tag{A16}$$

respectively, where the plasma dispersion function $Z(\hat{\omega})\equiv\pi^{-1/2}\int_{-\infty}^{\infty}d\alpha e^{-\alpha^2}/(\alpha-\hat{\omega})$ and the normalized frequency $\hat{\omega}\equiv R_0q\omega/\upsilon_{Ti}$ ($\upsilon_{Ti}\equiv\sqrt{2T_i/m_i}$) are used. Other Fourier components $\delta\hat{f}_{ik_r-10}$, $\delta\hat{f}_{ik_r-L0}$, $\delta\hat{f}_{ik_r,-L-n,-M}$, ϕ_{k_r-10}, ϕ_{k_r-L0}, and $\phi_{k_r,-L-n,-M}$ in Eq. (A9) are given by using Eqs. (A10)–(A16) and the following relations:

$$\begin{aligned}
&\delta\hat{f}_{ik_r-10}(\upsilon_\parallel)=-\delta\hat{f}_{ik_r10}(-\upsilon_\parallel),\\
&\delta\hat{f}_{ik_r-L0}(\upsilon_\parallel)=-\delta\hat{f}_{ik_rL0}(-\upsilon_\parallel),\\
&\delta\hat{f}_{ik_r,-L-n,-M}(\upsilon_\parallel)=-\delta\hat{f}_{ik_r,L+n,M}(-\upsilon_\parallel),\\
&\phi_{k_r-10}=-\phi_{k_r10},\\
&\phi_{k_r-L0}=-\phi_{k_rL0},\\
&\phi_{k_r,-L-n,-M}=-\phi_{k_r,L+n,M}.
\end{aligned} \tag{A17}$$

We now assume the initial perturbed ion gyrocenter distribution function to take the Maxwellian form $\delta f_{i\mathbf{k}_\perp}(t=0)=(\delta n_{i\mathbf{k}_\perp}^{(g)}(t=0)/n_0)F_{i0}$. Using the quasineutrality condition, the initial perturbed ion gyrocenter density is determined by $\delta n_{i\mathbf{k}_\perp}^{(g)}(t=0)=n_0(k_r^2a_i^2)(e\phi_{k_r00}(t=0)/T_i)$, where $\phi_{k_rlm}(t=0)=0$ for $(l,m)\neq(0,0)$ and $k_r^2a_i^2\simeq\langle k_\perp^2a_i^2\rangle\ll1$ are assumed. Substituting Eqs. (A10)–(A17) into Eq. (A9) and neglecting effects of $\delta\hat{I}_{ik_rlm}(\omega)$ as smaller than those of $\phi_{k_r00}(t=0)$ and S_{ik_r00} by the factor of k_ra_i, we can finally represent $\phi_{k_r00}(\omega)$ by

$$\frac{e\phi_{k_r00}(\omega)}{T_i}=\mathcal{K}_{\mathrm{GAM}}(\omega)\left[\frac{e\phi_{k_r00}(t=0)}{T_i}+\frac{\int d^3\upsilon F_{i0}S_{ik_r00}(\omega)}{n_0(k_ra_i)^2}\right], \tag{A18}$$

where $\mathcal{K}_{\mathrm{GAM}}(\omega)$ is defined by

$$\frac{1}{\mathcal{K}_{\mathrm{GAM}}(\omega)}\equiv-i\hat{\omega}-i\frac{q^2}{2}\left[\left(\frac{R_0\epsilon_{10}}{r}\right)^2\{J(\hat{\omega})+J_{\mathrm{FOW}}(\hat{\omega})\}+L\left(\frac{R_0\epsilon_{L0}}{r}\right)^2J\left(\frac{\hat{\omega}}{L}\right)\right.$$
$$\left.+\sum_{|n|\leqslant n_{\max}}\frac{(L+n)^2}{|L+n-qM|}\left(\frac{R_0\epsilon_h^{(n)}}{r}\right)^2\times J\left(\frac{\hat{\omega}}{|L+n-qM|}\right)\right], \tag{A19}$$

with

$$J(\hat{\omega})\equiv2\hat{\omega}^3+3\hat{\omega}+(2\hat{\omega}^4+2\hat{\omega}^2+1)Z(\hat{\omega})-\frac{\hat{\omega}}{2}\{2\hat{\omega}+(2\hat{\omega}^2+1)Z(\hat{\omega})\}^2\times\left\{\frac{T_i}{T_e}+1+\hat{\omega}Z(\hat{\omega})\right\}^{-1} \tag{A20}$$

and

$$J_{\mathrm{FOW}}(\hat{\omega})\equiv i\frac{\sqrt{\pi}}{2}\left(\frac{k_r\upsilon_{Ti}q}{\Omega_i}\right)^2e^{-\hat{\omega}_r^2/4}\times\left\{\frac{\hat{\omega}_r^6}{64}+\left(\frac{\hat{\omega}_r^4}{8}+\frac{3\hat{\omega}_r^2}{4}+3+\frac{6}{\hat{\omega}_r^2}\right)\times\left(1-\frac{3\hat{\omega}_r}{16}\{2\hat{\omega}_r+(2\hat{\omega}_r^2+1)Z_r(\hat{\omega}_r)\}\times\left\{\frac{T_i}{T_e}+1+\hat{\omega}_rZ_r(\hat{\omega}_r)\right\}^{-1}\right)\right\}. \tag{A21}$$

Here, J_{FOW} and the terms proportional to $(k_r\upsilon_{Ti}q/\Omega_i)^2\times\exp(-\hat{\omega}_r^2/4)$ on the right-hand side of Eq. (A14), where $\hat{\omega}_r=\mathrm{Re}(\hat{\omega})$, are derived from retaining the FOW effect on the $(l,m)=(\pm1,0)$ components of the ion gyrocenter distribution function as noted after Eq. (A6).

[1] P. H. Diamond, S.-I. Itoh, K. Itoh, and T. S. Hahm, Plasma Phys. Controlled Fusion **47**, R35 (2005).
[2] M. N. Rosenbluth and F. L. Hinton, Phys. Rev. Lett. **80**, 724 (1998).
[3] H. Sugama and T.-H. Watanabe, Phys. Rev. Lett. **94**, 115001 (2005).
[4] W. Horton, Rev. Mod. Phys. **71**, 735 (1999).
[5] A. M. Dimits, G. Bateman, M. A. Beer *et al.*, Phys. Plasmas **7**, 969 (2000).
[6] T.-H. Watanabe and H. Sugama, *20th IAEA Fusion Energy Conference* (Vilamoura, Portugal, 2004), TH/8-3Rb; "Velocity-space structures of distribution function in toroidal ion temperature gradient turbulence," Nucl. Fusion (to be published).
[7] N. Winsor, J. L. Johnson, and J. J. Dawson, Phys. Fluids **11**, 2248 (1968).

[8] A. Fujisawa, K. Itoh, H. Iguchi *et al.*, Phys. Rev. Lett. **93**, 165002 (2004).
[9] G. D. Conway, B. Scott, J. Schirmer, M. Reich, A. Kendl, and the ASDEX Upgrade Team, Plasma Phys. Controlled Fusion **47**, 1165 (2005).
[10] V. B. Lebedev, P. N. Yushmanov, P. H. Diamond, S. V. Novakovskii, and A. I. Smolyakov, Phys. Plasmas **3**, 3023 (1996).
[11] S. V. Novakovskii, C. S. Liu, R. Z. Sagdeev, and M. N. Rosenbluth, Phys. Plasmas **4**, 4272 (1997).
[12] T. Watari, Y. Hamada, A. Fujisawa, K. Toi, and K. Itoh, Phys. Plasmas **12**, 062304 (2005).
[13] H. Sugama and T.-H. Watanabe, *19th International Conference on Numerical Simulation of Plasmas and Seventh Asia Pacific Plasma Theory Conference* (Nara, Japan, 2005), A6-2; "Collisionless damping of geodesic acoustic modes," J. Plasma Phys. (submitted).
[14] S. Satake, M. Okamoto, N. Nakajima, H. Sugama, M. Yokoyama, and C. D. Beidler, Nucl. Fusion **45**, 1362 (2005).
[15] M. Wakatani, *Stellarator and Heliotron Devices* (Oxford University Press, Oxford, 1998), Chap. 7.
[16] K. C. Shaing and S. A. Hokin, Phys. Fluids **26**, 2136 (1983).
[17] O. Motojima, N. Ohyabu, A. Komori *et al.*, Nucl. Fusion **43**, 1674 (2003).
[18] H. Yamada, A. Komori, N. Ohyabu *et al.*, Plasma Phys. Controlled Fusion **43**, A55 (2001).
[19] T. Kuroda and H. Sugama, J. Phys. Soc. Jpn. **70**, 2235 (2001).
[20] G. Rewoldt, L.-P. Ku, W. M. Tang, H. Sugama, N. Nakajima, K. Y. Watanabe, S. Murakami, H. Yamada, and W. A. Cooper, Nucl. Fusion **42**, 1047 (2002).
[21] F. L. Hinton and M. N. Rosenbluth, Plasma Phys. Controlled Fusion **41**, A653 (1999).
[22] E. A. Frieman and L. Chen, Phys. Fluids **25**, 502 (1982).
[23] R. D. Hazeltine and J. D. Meiss, *Plasma Confinement* (Addison-Wesley, Redwood City, CA, 1992), p. 298.
[24] D. A. Spong, Phys. Plasmas **12**, 056114 (2005).